OPEN ACCESS



Detection of Thermal Sunyaev–Zel'dovich Effect in the Circumgalactic Medium of Lowmass Galaxies—A Surprising Pattern in Self-similarity and Baryon Sufficiency

Sanskriti Das^{1,2}, Yi-Kuan Chiang^{3,4}, and Smita Mathur^{2,4}

¹ Kavli Institute for Particle Astrophysics and Cosmology, Stanford University, 452 Lomita Mall, Stanford, CA 94305, USA; snskriti@stanford.edu
² Department of Astronomy, The Ohio State University, 140 West 18th Avenue, Columbus, OH 43210, USA
³ Institute of Astronomy and Astrophysics, Academia Sinica, Astronomy-Mathematics Building, No. 1, Section 4, Roosevelt Road, Taipei 10617, Taiwan
⁴ Center for Cosmology and Astroparticle Physics, 191 West Woodruff Avenue, Columbus, OH 43210, USA
Received 2023 February 20; revised 2023 May 11; accepted 2023 May 19; published 2023 July 7

Abstract

We report on the measurement of the thermal Sunyaev–Zel'dovich (tSZ) effect in the circumgalactic medium (CGM) of 641,923 galaxies with $M_{\star}=10^{9.8-11.3}M_{\odot}$ at z<0.5, pushing the exploration of the tSZ effect to lower-mass galaxies compared to those in previous studies. We cross-correlate the galaxy catalog of the Wide-field Infrared Survey Explorer and SuperCOSMOS with Compton-y maps derived from the combined data of the Atacama Cosmology Telescope and Planck. We improve on the data analysis methods (correcting for cosmic infrared background and Galactic dust, masking galaxy clusters and radio sources, stacking, and employing aperture photometry), as well as modeling (taking into account beam smearing, the "two-halo" term, and any zero-point offset). We constrain the thermal pressure in the CGM of $M_{\star}=10^{10.6-11.3}M_{\odot}$ galaxies for a generalized Navarro–Frenk–White profile and provide upper limits for $M_{\star}=10^{9.8-10.6}M_{\odot}$ galaxies. The relation between M_{500} (obtained from an empirical $M_{\star}-M_{200}$ relation and a concentration factor) and $\tilde{Y}_{R500}^{\rm sph}$ (a measure of the thermal energy within R_{500}) is $>2\sigma$ steeper than the self-similarity relation and the deviation from the same that has been reported previously in higher-mass halos. We calculate the baryon fraction of the galaxies, f_b , assuming the CGM to be at the virial temperature that is derived from M_{200} . The baryon fraction f_b exhibits a nonmonotonic trend with mass, with $f_{\star}=10^{10.9-11.2}M_{\odot}$ galaxies being baryon-sufficient.

Unified Astronomy Thesaurus concepts: Circumgalactic medium (1879); Hot ionized medium (752); Hot intergalactic medium (751); Sunyaev-Zeldovich effect (1654); Millimeter astronomy (1061); Cosmic microwave background radiation (322); Extragalactic astronomy (506); Galaxy evolution (594); Galactic winds (572); Galaxy processes (614); Galaxy environments (2029); Observational cosmology (1146)

1. Introduction

The circumgalactic medium (CGM) is the multiphase halo of gas and dust surrounding the stellar disk and the interstellar medium of a galaxy (Putman et al. 2012; Tumlinson et al. 2017; Mathur 2022; Faucher-Giguere & Oh 2023). As a nexus of accretion from the intergalactic medium (IGM), galactic outflow, and recycling precipitation, the CGM plays a crucial role in the formation and evolution of a galaxy and might harbor the missing galactic baryons (Cen & Ostriker 1999). The most massive and volume-filling phase of the CGM is predicted to be ≥10⁶ K hot and fully ionized (e.g., Spitzer 1956; Schaye et al. 2015; Hopkins et al. 2018; Nelson et al. 2018; Li & Tonnesen 2020). This hot gas can be observed in the emission and absorption lines of highly ionized (He-like or H-like) metal ions and free–free continuum emission in X-ray (Mathur 2022), and in the Sunyaev–Zel'dovich (SZ) effect (Sunyaev & Zeldovich 1969; Mroczkowski et al. 2019).

The SZ effect is a distortion in the spectrum of the cosmic microwave background (CMB) due to the inverse Compton scattering of CMB photons with free electrons in the intervening ionized medium (Sunyaev & Zeldovich 1969). The thermal SZ (tSZ) effect, the strongest of different SZ effects, is characterized by the Compton-y parameter: $y = (\sigma_{\rm T}/m_e c^2) \int P_e dl$. It is a

Original content from this work may be used under the terms of the Creative Commons Attribution 4.0 licence. Any further distribution of this work must maintain attribution to the author(s) and the title of the work, journal citation and DOI.

measure of the thermal pressure ($P_e = n_e k_B T_e$) or thermal energy density of the free electrons of the relevant medium integrated along the line of sight. If the physical properties of the halo gas are driven by the gravitational potential, the thermal energy of the halo gas ($\propto \int P_e dV \propto \int y dA$) would solely depend on the virial mass of the halo—referred to as self-similarity. However, simulations predict that self-similarity breaks in low-mass halos as the role of galactic feedback becomes increasingly important compared to the gravitation (e.g., Lim et al. 2021; Kim et al. 2022; Pop et al. 2022).

The hot CGM of the Milky Way has been extensively observed in X-ray emission (e.g., Snowden et al. 2000; Henley et al. 2010; Das et al. 2019a; Kaaret et al. 2020; Gupta et al. 2021; Bluem et al. 2022; Bhattacharyya et al. 2023; Gupta et al. 2023) and X-ray absorption (e.g., Williams et al. 2005; Gupta et al. 2012; Nicastro et al. 2016; Gatuzz & Churazov 2018; Das et al. 2019c, 2021a; Lara-DI et al. 2023). It is incredibly challenging to probe the hot CGM of external galaxies in emission due to the spatially and temporally variable foreground dominating the total X-ray emission. So far, extended emission from the hot CGM has been detected around a handful of individual massive $(M_{\star} > 10^{11.3} M_{\odot})$ super- L^{\star} galaxies (e.g., Anderson et al. 2016; Bogdán et al. 2017; Li et al. 2017) and one external L^* galaxy (Das et al. 2019b, 2020). There have also been stacking efforts to detect the CGM in emission by cross-correlating the eROSITA data with galaxy catalogs at z < 0.1 (Chadayammuri et al. 2022; Comparat et al. 2022).

However, X-ray emission is biased toward gas at higher density and higher emissivity, and thus it is primarily sensitive

 $^{^{5}}$ $\sigma_{\rm T}$, m_e , and c are the Thomson scattering cross section, the rest mass of the electron, and the speed of light in vacuum, respectively.

to the inner region of the CGM. X-ray absorption is not affected by the bias mentioned above, but it has sparse spatial sampling due to pencil beams. Also, X-ray absorption entirely depends on metal ions, which makes results dependent on the assumed abundance ratios of metals and the metal-to-hydrogen ratio. In addition to that, the lack of sufficient X-ray-bright QSO sightlines passing through the CGM of external galaxies limits the scope to probe the hot CGM of external galaxies in absorption (e.g., Mathur et al. 2021; Nicastro et al. 2023).

The SZ effect, on the other hand, does not suffer from the observational biases of X-ray emission, or the restricted spatial coverage and metallicity dependence of X-ray absorption. Also, the redshift independence of the SZ effect allows one to study the CGM across cosmic time. Therefore, use of the SZ effect is a powerful technique to characterize the CGM and test self-similarity in the halo of galaxies, complementary to X-ray observations.

Unlike spectroscopy, use of the tSZ effect cannot distinguish between the hot CGM and the partially ionized cool/warm (10^{4-6} K) CGM. However, the hot CGM has a higher temperature (T_e) and higher dispersion measure (DM = $\int n_e dl$) compared to the cooler phases of the CGM (e.g., the hot CGM of the Milky Way contributes to the DM of the Galactic halo ≈ 1 order of magnitude more than all the other phases of the CGM combined; see Das et al. 2021b). That makes the hot CGM the primary contributor to the tSZ effect of any galaxy halo.

Using Planck data, detection of the tSZ effect has been reported in the CGM of massive $(M_{\star}>10^{11.3}M_{\odot})$ locally brightest galaxies (LBGs) and galaxy groups at $z\lesssim0.1$ (Planck Collaboration et al. 2013; Greco et al. 2015; Lim et al. 2018) and the large-scale structure of the universe up to z=1 (Chiang et al. 2020, 2021). Recently, the combined maps of the Atacama Cosmology Telescope (ACT) + Planck and the South Pole Telescope + Planck have been cross-correlated with galaxy catalogs at $0.5\leqslant z\leqslant1.5$, again focusing on massive galaxies and galaxy groups (Meinke et al. 2021; Schaan et al. 2021; Vavagiakis et al. 2021; Pandey et al. 2022).

Building on these works, we extend the search for the tSZ effect in the CGM of lower-mass galaxies. In Section 2, we discuss the data extraction and data analysis. The results and their physical interpretation are mentioned in Section 3. We conclude and summarize our results in Section 4.

We use the flat Λ CDM cosmology of Planck Collaboration et al. (2016) throughout the paper: local expansion rate $H_0=67.7~{\rm km\,s^{-1}~Mpc^{-1}}$, matter density $\Omega_m=0.307$, baryon density $\Omega_b=0.0486$, and dark energy density $\Omega_\Lambda=1-\Omega_m=0.693$. The cosmological baryon fraction $f_{b,{\rm cosmo}}=\Omega_b/\Omega_m$ is 0.158. Virial parameters are expressed in terms of overdensity Δ , e.g., $M_\Delta=\frac{4}{3}\pi R_\Delta^3\Delta\rho_c(z)$ is the mass enclosed within a sphere of radius R_Δ , where the mean mass density is Δ times the critical density of the universe, $\rho_c(z)=3H(z)^2/8\pi G$. H(z) is the Hubble parameter at redshift z, and G is the Newtonian constant of gravitation. The redshift evolution of the Hubble parameter is $E(z)^2=H(z)^2/H_0^2=\Omega_m\times(1+z)^3+\Omega_\Lambda$.

2. Data Extraction and Analyses

2.1. Compton-y Maps

We obtain Compton-y maps constructed by using a component separation method based on the internal linear combination approach from Madhavacheril et al. (2020, hereafter M20). These

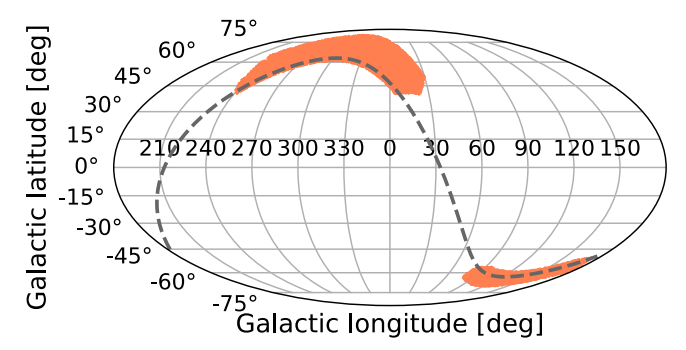


Figure 1. Positions of the Compton-y maps (red patches) in a Mollweide projection of galactic coordinates. BN and D56 are in the northern and southern hemispheres, respectively. The equatorial plane is shown as a dashed gray curve.

maps are extracted from the multifrequency data of ACTPol DR4 (98 and 150 GHz) and Planck (30, 44, 70, 100, 143, 217, 353, and 545 GHz). These maps are derived in two distinct, nonoverlapping patches of the sky: BN (-117° < R.A. < 150°, -2° < decl. < 19°; area = 1633 deg²) and D56 (-9° < R.A. < 40°, -7° < decl. < 4°; area = 456 deg²), shown in Figure 1. At small scales (multipole l > 1000) these y-maps are dominated by the ACT data. These maps cover only 5% of the sky, but the signal-to-noise ratio on small scales is orders of magnitude higher than those of previous Planck-based y-maps. Also, the smaller beam size of ACT (FWHM \approx 1′) compared to Planck (FWHM \approx 10′) allows us to resolve the galaxy halos at a smaller angular size than before.

To understand the effect of thermal dust on the Compton-y measurements, we use two types of the y-maps from M20 in our analyses—maps before and after the deprojection of the cosmic infrared background (CIB). The spectral energy distribution (SED) of the CIB is modeled as a modified blackbody with $T_{\rm CIB}=24~\rm K$, consistent with the all-sky average of the SED fit to the CIB power spectrum measurements from Planck. The FWHMs of the Gaussian beams relevant for the y-maps before and after CIB deprojection are 1.6 and 2.4, respectively.

2.1.1. Galactic Dust

We test if the *y*-maps are affected by Galactic dust. Because the characteristic angular scales of the CIB and Galactic dust are not necessarily the same, the *y*-maps after CIB correction might have residual contamination by Galactic dust emission. Therefore, we consider the *y*-maps both before and after CIB correction. $N(\text{H I})_{\text{Gal}}$, the neutral hydrogen column density of the Galaxy, linearly correlates with E(B-V), the reddening due to Galactic dust (Lenz et al. 2017). Therefore, we use $N(\text{H I})_{\text{Gal}}$ as a substitute for Galactic dust in our analyses. We obtain $N(\text{H I})_{\text{Gal}}$ from the HI4PI survey (HI4PI Collaboration et al. 2016) and construct $N(\text{H I})_{\text{Gal}}$ maps for the sky regions BN and D56.

In the scenario of negligible contamination by Galactic dust, Compton-y values would be uncorrelated with $N({\rm H\,I})_{\rm Gal}$. We find that the pixelwise Compton-y values are unlikely to be correlated with $N({\rm H\,I})_{\rm Gal}$ (Spearman correlation coefficients $|C_{\rm Sp}| < 0.1$; 2D histograms in Figure 2). However, the mean Compton-y shows a strong negative correlation with the mean $N({\rm H\,I})_{\rm Gal}$ ($|C_{\rm Sp}| > 0.9$) in both patches of the sky, both before and after CIB correction (Figure 2, red lines). The correlation becomes stronger at high $N({\rm H\,I})_{\rm Gal}$. The unphysical negative

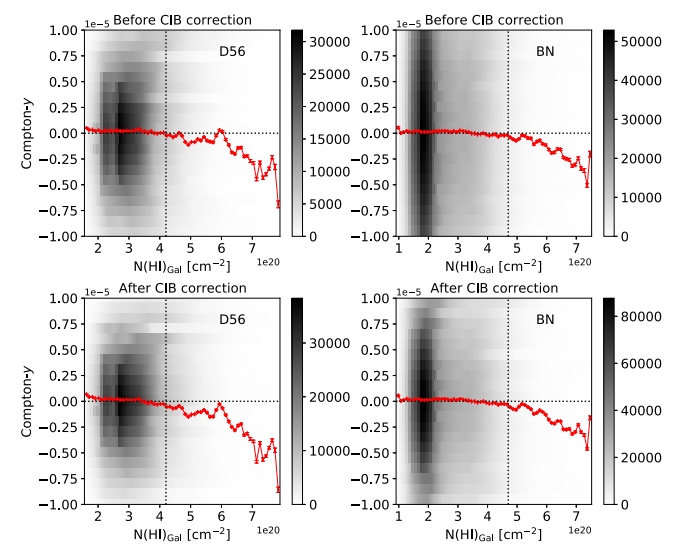


Figure 2. Compton-y values before (top) and after (bottom) CIB correction as a function of Galactic $N(H \ I)$ in the sky regions of D56 (left) and BN (right). The color bars denote the number of pixels in the y-maps at the corresponding values of Compton-y and $N(H \ I)_{Gal}$ in the 2D histograms. The mean Compton-y as a function of the mean $N(H \ I)_{Gal}$ are calculated at a constant bin width of $10^{19} \ \text{cm}^{-2}$; these are shown as red points and red curves. The vertical dotted lines are drawn at the $N(H \ I)_{cut}$ that we implement in our analyses. The horizontal dotted lines are drawn at y = 0 to guide the eye.

values of the mean Compton-y at high $N(H I)_{Gal}$ and the persisting correlation after CIB correction imply that the contribution of Galactic dust has not been completely accounted for in the process of CIB correction.

To minimize the effect of Galactic dust in further analyses, we exclude pixels in the *y*-maps corresponding to $N({\rm H~I})_{\rm Gal}$ above a certain $N({\rm H~I})_{\rm cut}$ based on the following conditions. The remaining mean *y*-values are in the order of 10^{-7} within errors, and the correlation between the mean Compton-*y* and the mean $N({\rm H~I})_{\rm Gal}$ becomes weaker, while we can retain most (>95%) of the data. We use $N({\rm H~I})_{\rm cut}$ of 4.7×10^{20} cm⁻² and 4.2×10^{20} cm⁻² for the sky regions BN and D56, respectively.

2.2. Galaxy Sample

In order to cross-correlate with the Compton-y maps, we consider the Wide-field Infrared Survey Explorer (WISE) × SCOSPZ galaxy catalog, which was constructed by crossmatching the all-sky samples of WISE and SuperCOS-MOS and whose photometric redshifts were estimated using an artificial neural network algorithm (Bilicki et al. 2016). We extract the sky location, photometric redshift $z_{\rm ph}$, and Galactic dust extinction–corrected WISE 3.4 μ m (W1) and 4.6 μ m (W2) magnitude of the galaxies in the BN and D56 regions from the galaxy catalog. The catalog excludes targets with W1 – W2 > 0.9, thus making sure that the galaxies in the catalog are unlikely to host active nuclei.

We calculate stellar masses from the W1 and W2 magnitude using the scaling relation from Cluver et al. (2014). The redshift distribution of the stellar masses is shown in Figure 3. Because detection of the tSZ effect has been previously reported in the CGM of $M_{\star} > 10^{11.3} M_{\odot}$ galaxies, we focus on galaxies of lower stellar mass: $9.8 \leq \log(M_{\star}/M_{\odot}) \leq 11.3$. The median redshift and the median stellar mass of our sample are 0.2 and $10^{10.48} M_{\odot}$, respectively.

The sky regions BN and D56 are unlikely to be contaminated by stars in the Galactic disk due to their high galactic latitude

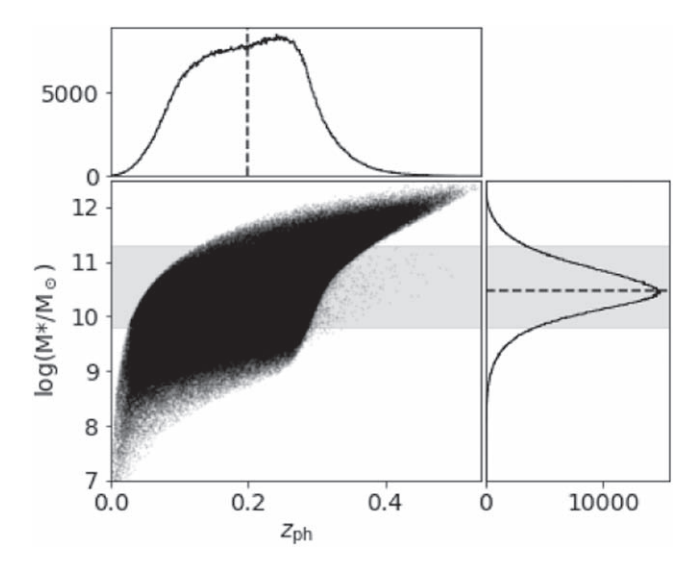


Figure 3. The redshift distribution of the stellar masses of our galaxy sample. The horizontal and vertical dashed lines denote the median of the stellar mass and the redshift, respectively. The range of stellar masses considered in this paper, $9.8 \le \log(M_*/M_{\odot}) \le 11.3$, is highlighted with a horizontal gray band.

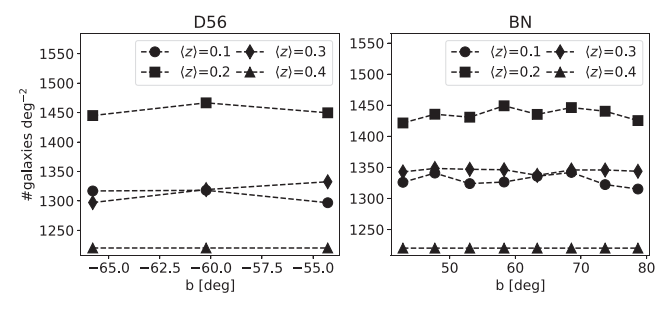


Figure 4. The surface density distribution of the $9.8 \le \log(M_*/M_{\odot}) \le 11.3$ galaxies as a function of the galactic latitude and the redshift of the galaxies.

 $(|b|>30^\circ)$; see Figure 1). To test if it is otherwise, we calculate the surface density, i.e., the number of galaxies per unit area of the sky as a function of the galactic latitude and the redshift of the galaxies (Figure 4). If the galaxy sample is predominantly contaminated by stars, the surface density would be anticorrelated with the galactic latitude. But the surface density is practically uniform, with <10% fluctuation (Figure 4). At a given galactic latitude the surface density follows the redshift distribution shown in Figure 3, but it is not correlated with the galactic latitude at a given redshift. It confirms that our galaxy sample is not contaminated by stars in the Galactic disk.

We estimate the virial (or halo) masses of the galaxies, $M_{\rm vir}$ ($\equiv M_{200}$), from the stellar masses using the stellar-to-halo mass relation (SHMR) from Zu & Mandelbaum (2015, hereafter Z15). The behavior of the empirical model of Z15 is governed by the results of Behroozi et al. (2010), but Z15 have refitted the parameters to the z=0 data of Sloan Digital Sky Survey Data Release 7, and allowed the scatter around the best fit to vary with halo mass. We calculate the virial radii $R_{\rm vir}$ ($\equiv R_{200}$) using the Navarro–Frenk–White (NFW) profile of the dark matter (Navarro et al. 1997). We also determine the corresponding angular size $\theta_{\rm vir}$ ($\equiv \theta_{200} = R_{200}/D_A$, where D_A is the angular diameter distance). Using the concentration factor c_{200} as a function of the virial mass (Neto et al. 2007), we convert M_{200} to M_{500} and obtain the corresponding R_{500} as well.

2.3. Masking

The tSZ effect of the intracluster medium (ICM) and the emission from compact radio sources can contaminate/bias our Compton-y measurements. Therefore, we mask the y-maps at the positions of galaxy clusters and radio sources. We discuss the removal process in the following sections.

2.3.1. Galaxy Clusters

We extract the position, redshift, and virial mass $M_{200,cl}$ of galaxy clusters from a tSZ cluster catalog (Hilton et al. 2021). These clusters have been individually detected at $>4\sigma$ in the 98 and 150 GHz channels of ACT, and have been optically confirmed. We calculate the virial radii, $R_{200,cl}$, using the NFW profile of dark matter. We determine the angular size $\theta_{200,cl}$ of the cluster halos from their $R_{200,cl}$ and redshift. We exclude (\equiv NaN) the $\theta_{200,cl}$ regions around the clusters in the y-maps. The cluster catalog does not include the nearby Virgo cluster and the A119 cluster, which are prominently visible in the ymaps. We obtain the $R_{200,cl}$ and the redshift of these clusters from Kashibadze et al. (2020) and Piffaretti et al. (2011), respectively, and remove the corresponding $\theta_{200,cl}$ regions around them. Galaxies in our sample that reside within these clusters are naturally removed in this process. Because field galaxies and galaxies within clusters evolve in different environments, their tSZ effects might be different from each other. The exclusion of galaxies within clusters will make the interpretation of our results more straightforward.

2.3.2. Radio Sources

Our goal is to remove radio sources from the *y*-maps down to the 1σ noise level at 98 and 150 GHz. We translate the corresponding flux at these frequencies to the flux at ≈ 1.4 GHz, $F_{1.4}$, using the median SED of $F_{\nu} \propto \nu^{-0.75}$ for radio-loud quasars (Shang et al. 2011). We exclude (\equiv NaN) regions in the *y*-maps affected by radio sources brighter than $F_{1.4}$, i.e., the angular size of sources convolved with Gaussian beams relevant for the *y*-maps (see Section 2.1).

We crossmatch the WISE \times SCOSPZ catalog with the FIRST catalog, and find that $\approx 0.4\%$ of the WISE \times SCOSPZ galaxies of our interest are radio-loud; we exclude them from our galaxy sample.

2.4. Stacking

We split the galaxy sample into stellar mass bins of different widths, $\Delta M_{\star} = 0.2$ dex, 0.3 dex, and 0.4 dex, and stack the Compton-y map in each mass bin separately. With wide mass bins, we can constrain the value of Compton-y at higher significance. On the other hand, we get better insight into the mass dependence of Compton-y from the narrow mass bins. We provide the stellar mass, mean redshift, total number of galaxies, mean virial mass, and virial radius in each mass bin in Table 1. We perform the same procedure for both patches of the sky and then combine them.

We stack the *y*-maps in three ways, at (i) a fixed angular size, (ii) a fixed projected radius, and (iii) a fixed fraction of virial radius; these are discussed in detail below.

(i) Fixed angular size. Following most previous studies, we stack stamps⁷ of a fixed angular size:

$$y_{\text{stacked}} = \langle y(\theta_i) \rangle; \ \theta_i = \theta_{\perp} = r_i / D_{A,i}.$$
 (1)

Here, r_i and $D_{A,i}$ are the projected radius and the angular diameter distance of the *i*th galaxy in the subsample, respectively; $\langle y \rangle$ is the average Compton-y value of all galaxies in that subsample at a fixed galactocentric angular distance perpendicular to the line of sight, θ_{\perp} . We extract each stamp out to the median $6 \times \theta_{200}$ of the relevant subsample so that we can study y out to a sufficiently large angular separation beyond the CGM, and estimate the tSZ background from the same stamp.

For galaxies at different redshifts, this method stacks different projected radii, which also means different fractions of R_{200} for galaxies of similar halo masses. Thus, it is not straightforward to extract any physically meaningful information for the galaxies from the stacking at a given angular size. For this reason, we introduce the other two stacking procedures.

(ii) Fixed projected radius. Here, the galaxy halos are stacked at the same projected radius:

$$y_{\text{stacked}} = \langle y(\theta_i) \rangle; \ \theta_i = r_{\perp}/D_{A,i}.$$
 (2)

Here $\langle y \rangle$ is the average Compton-y value of all galaxies in the subsample at a fixed galactocentric physical distance perpendicular to the line of sight, r_{\perp} . This method works under the assumption that the radial pressure profiles of the CGM, P(r), have the same shape in all galaxies in a subsample.

We extract each stamp out to the median $6 \times R_{200}$ in the relevant mass bin. Because the corresponding angular size of the stamp is not the same for each galaxy, the stamps have different numbers of pixels, $n_{\rm pixel}$, on each side, which cannot be directly stacked. Therefore, we reconstruct each stamp using 2D piecewise linear interpolation so that all stamps have the same $n_{\rm pixel}$. Thus, the stamps are under- or oversampled when the initial $n_{\rm pixel}$ is larger or smaller than the final $n_{\rm pixel}$, respectively. The final $n_{\rm pixel}$ is set to the median of the initial $n_{\rm pixel}$ distribution of all stamps, corresponding to the angular size at the median D_A of the subsample. Thus, half of the stamps are undersampled and the other half are oversampled, minimizing the effects of the stamp reconstruction. The

⁶ A fraction of the radio sources are stellar or unclassified and may have a different SED than the radio galaxies. Our goal is to exclude the brightest sources, and galaxies are brighter than other sources, validating our assumption of the SED.

We call a cutout of the y-map around a galaxy a "stamp." It is extracted using the thumbnail subroutine of the reprojection module of pixell (Naess et al. 2021). Each "stamp" is projected onto a local tangent plane in order to remove the effect of size and shape distortions in the input y-map.

Table 1
Properties of Our Galaxy Sample and the Corresponding tSZ Effect

$\frac{\log(M_{\star})}{(M_{\odot})}$	# of Galaxies	Z	$\log(M_{200})$ (M_{\odot})	R ₂₀₀ (kpc)	$R_{\min} \atop (R_{200})$	$\tilde{Y}_{R500}^{\text{sph}}$ $(\times 10^{-8} \text{arcmin}^2)$	$M_{\rm gas,200} \times 10^{11} M_{\odot})$
(1)	(2)	(3)	(4)	(5)	(6)	(7)	(8)
			$\Delta M_{\star} = 0.3$	dex			
9.8–10.1	93,907	0.158 ± 0.063	11.86 ± 0.04	185 ± 5	1.09	< 5.86	<2.85
10.1-10.4	175,255	0.172 ± 0.061	12.00 ± 0.05	206 ± 7	1.05	< 5.26	< 2.74
10.4-10.7	187,761	0.192 ± 0.060	12.18 ± 0.07	237 ± 12	0.99	< 6.28	< 2.74
10.7-11.0	124,892	0.233 ± 0.056	12.43 ± 0.09	287 ± 19	0.94	8.1 ± 4.6	1.51 ± 1.31
10.8-11.1	101,155	0.249 ± 0.053	12.53 ± 0.10	310 ± 21	0.92	17.3 ± 6.1	2.79 ± 1.34
10.9-11.2	79,367	0.265 ± 0.050	12.64 ± 0.10	336 ± 25	0.88	34.2 ± 8.6	4.73 ± 1.55
11.0-11.3	60,108	0.281 ± 0.047	12.75 ± 0.11	366 ± 29	0.84	37.3 ± 11.0	4.37 ± 1.71
			$\Delta M_{\star} = 0.2$	dex			
10.6–10.8	106,715	0.211 ± 0.059	12.31 ± 0.05	261 ± 10	0.97	<11.75	<3.61
10.7-10.9	91,250	0.226 ± 0.057	12.40 ± 0.06	279 ± 11	0.95	<18.58	<4.77
10.8-11.0	75,326	0.242 ± 0.054	12.50 ± 0.06	301 ± 13	0.93	15.3 ± 6.8	2.61 ± 1.30
10.9-11.1	59,469	0.258 ± 0.050	12.60 ± 0.07	326 ± 15	0.90	31.1 ± 9.3	4.55 ± 1.55
11.0-11.2	45,726	0.274 ± 0.047	12.71 ± 0.07	355 ± 18	0.86	30.8 ± 11.7	3.84 ± 1.96
11.1–11.3	34,280	0.290 ± 0.044	12.83 ± 0.07	389 ± 21	0.82	47.1 ± 15.9	4.93 ± 2.16
			$\Delta M_{\star} = 0.4$	dex			
10.5–10.9	212,095	0.210 ± 0.060	12.29 ± 0.11	258 ± 20	0.97	<7.21	<2.58
10.6–11.0	182,042	0.225 ± 0.058	12.38 ± 0.12	275 ± 23	0.95	5.8 ± 3.2	1.17 ± 0.92

Notes. The number of galaxies, the mean redshift, the mean virial mass, and the mean virial radius with 1σ scatters in each stellar mass bin are quoted in the second to fifth columns. R_{\min} denotes the smallest aperture in units of R_{200} . The error bars in \tilde{Y} and M_{gas} are 1σ and the upper limits (for values constrained at <90% confidence) are 3σ . M_{gas} is calculated assuming the CGM is at virial temperature.

distance of a given pixel from the central pixel in a reconstructed stamp is equivalent to the projected physical distance between the corresponding sky point and the center of the relevant galaxy.

(iii) Fixed fraction of virial radius. Here, we stack the galaxy halos at the same fraction of R_{200} of each galaxy:

$$y_{\text{stacked}} = \langle y(\theta_i) \rangle; \ \theta_i = r_i / D_{A,i}; \ r_i = f_{200} \times R_{200,i}.$$
 (3)

Here $\langle y \rangle$ is the average Compton-y value at galactocentric physical distances perpendicular to the line of sight, r_i , which are a given fraction, f_{200} , of $R_{200,i}$, the virial radius of the *i*th galaxy in the relevant mass bin. This method works under the assumption that the radial pressure profiles of the CGM are self-similar, i.e., the pressure at a given fraction of R_{200} , $P(f_{200})$, has the same shape in all galaxies that are being stacked.

We extract the stamp out to $6 \times R_{200}$ of each galaxy. Because the corresponding angular size, $6 \times \theta_{200}$, is different for each galaxy, we follow the same steps of reconstructing y-maps as those of the previous method of stacking. The final $n_{\rm pixel}$, the same as the median of the initial $n_{\rm pixel}$ distribution, corresponds to the median $6 \times \theta_{200}$ of the subsample. The distance of a given pixel from the central pixel in a reconstructed stamp is equivalent to the projected distance of the corresponding sky point from the relevant galaxy center in units of R_{200} .

For galaxies at similar redshifts, the first and the second stacking method would produce the same result. For galaxy samples with similar R_{200} , the second and the third stacking method would be equivalent. For galaxies at similar redshifts and with similar R_{200} , the third stacking method would converge to the first one.

2.5. Aperture Photometry

We extract the radial profile of Compton-y from the stacked y-maps in two different ways: cumulative (the conventional method), and differential. As such, these provide us with complementary information.

The differential profile is a direct way to detect the signal at any projected distance. In the absence of a signal, the differential profile would be consistent with zero. We define the differential profile in Equation (4a):

$$y(\theta_{\rm df}) = \bar{y}_{\rm stacked}(\theta_{\rm df} - \Delta\theta \leqslant \theta_{\perp} < \theta_{\rm df} + \Delta\theta).$$
 (4a)

Here, $\theta_{\rm df}$ and $2\Delta\theta$ are the angular size and width of the circular annulus, respectively; $2\Delta\theta$ is the FWHM of the Gaussian beam so that each annulus is just resolved; and \bar{y} is the average y within the annulus. For stacking method (ii),

$$\theta_{\rm df} = r_{\perp,\rm df}/D_{\rm A,med}; \Delta\theta = \Delta r/D_{\rm A,med}.$$
 (4b)

Here, $r_{\perp,\rm df}$ and $2\Delta r$ are the physical radius and width of the circular annulus, and $D_{A,\rm med}$ is the median angular diameter distance of the galaxy subsample. For the third stacking method,

$$\theta_{\rm df} = f_{\rm df} \times \theta_{200,\rm med}; \ \Delta\theta = \Delta f \times \theta_{200,\rm med}.$$
 (4c)

Here, $f_{\rm df}$ and $2\Delta f$ are the physical radius and width of the annulus in units of R_{200} , and $\theta_{200,\rm med}$ is the median angular size of the galaxy halos in the subsample.

The cumulative profile is an indirect way to detect the signal, especially when the data is not deep enough for us to directly detect the signal. We define the cumulative profile in

Equation (5a):

$$y(\theta_{\rm cm}) = \bar{y}_{\rm stacked}(\theta_{\perp} \leqslant \theta_{\rm cm})$$

$$Y(\theta_{\rm cm}) = \int_{0}^{\theta_{\rm cm}} y d\Omega = y(\theta_{\rm cm}) \times \pi \theta_{\rm cm}^{2}.$$
 (5a)

Here θ_{cm} is the angular radius of the circular aperture, and \bar{y} is the average y within the aperture. For stacking methods (ii) and (iii),

$$\theta_{\rm cm} = r_{\perp,\rm cm}/D_{\rm A,med}$$
 (5b)

and

$$\theta_{\rm cm} = f_{\rm cm} \times \theta_{200,\rm med}.$$
 (5c)

Here $r_{\perp,\text{cm}}$ is the physical radius of the aperture, and f_{cm} is the radius of the aperture in units of R_{200} .

The minimum value of $\theta_{\rm cm}$ and $(\theta_{\rm df}+\Delta\theta)$ by definition is half of the FWHM of the relevant Gaussian beam because any region smaller than this is not resolvable. For each mass bin it is indicated in Table 1 in units of the virial radius. The maximum $\theta_{\rm cm}$ and $(\theta_{\rm df}+\Delta\theta)$ depend on the stamp size, which, as described in Section 2.4, is the median $6\sqrt{2}\times\theta_{200}$, median $6\sqrt{2}\times R_{200}/D_{A,\rm med}$, and median $6\sqrt{2}\times\theta_{200}$ of the relevant galaxies in stacking methods (i), (ii), and (iii), respectively.

Equation (5a) is different from the cumulative estimate that was used in previous studies of the tSZ effect (e.g., Schaan et al. 2021). For an aperture of angular size θ , they extracted the background from the region between θ and $\sqrt{2}\,\theta$ and subtracted it from the signal. In our case, the shape of the cumulative profile is more informative than the absolute values. In the presence of any signal, the cumulative profile should monotonically increase with radius, and the rate of increase would indicate the strength of the signal in the outer part of the aperture. The profile would saturate when there is no signal.

2.6. Error Estimation

We estimate the combined statistical and systematic uncertainties in the Compton-y using the bootstrap method. For a sample of N galaxies, we create a replica of the sample by replacing one galaxy with a randomly chosen galaxy from the rest of the galaxies in that sample (N-1). For every stacked sample, we make a set of 1000 such replicas and obtain the mean, covariance matrix, and 68.27% and 99.73% confidence intervals of the distribution of those replicas.

2.7. tSZ Background

For the following calculation, we consider the radial profiles of Compton-y, y_{tot} , derived from the CIB and Galactic dust-corrected, galaxy cluster and radio source-masked stacked y-maps. The radial profile of y_{tot} has two components, the "one-halo" radial profile of Compton-y, y_{1h} , and the tSZ background. This background consists of the "two-halo" term, y_{2h} , and any zero-point offset, y_{zp} . The "two-halo" term is the correlated tSZ signal of other halos around the galaxy of interest. The offset y_{zp} comprises the global Compton-y signal arising from reionization, the IGM, the CGM of the Milky Way, and calibration uncertainties. We consider the "two-halo" term calculated for an FWHM=1.'4 beam from Vikram et al. (2017), and add it to y_{1h} in each radial bin with a variable amplitude,

 A_{2h} (Equation (6)):

$$y_{\text{tot}}(r_{\perp}) = y_{1h}(r_{\perp}) + A_{2h}y_{2h}(r_{\perp}) + y_{zp}.$$
 (6)

2.8. Modeling Pressure and tSZ

In the observed tSZ effect, the thermal pressure of free electrons in the CGM, $P_e(r)$, is convolved with the effective beam of the y-maps that we use in the stacking:

$$y_{1h}(r_{\perp}) = (\sigma_{T}/m_{e}c^{2}) \int_{-\infty}^{\infty} P_{e}(r)dl \circledast \operatorname{Beam}(r_{\perp})$$
where $r^{2} = r_{\perp}^{2} + l^{2}$,
$$\operatorname{Beam}(\theta) = \frac{1}{\sqrt{2\pi}\sigma} \exp(-\theta^{2}/2\sigma^{2}),$$
and $\sigma = \operatorname{FWHM}/2\sqrt{2\ln(2)}$. (7)

Here, r_{\perp} and l are the physical distances perpendicular to and along the line of sight, respectively.

We model $P_e(r)$ with a generalized NFW (GNFW) profile (Equation (8)) that was first defined by Nagai et al. (2007) to describe the ICM:

$$\begin{split} P_e(x) &= P_{500} \Big(\frac{M_{500}}{3 \times 10^{14} h_{70}^{-1} M_{\odot}} \Big)^{\alpha_p + \alpha_p'(x)} \mathbb{P}(x) \\ \text{where } x &= r/R_{500}, \\ P_{500} &= 500 \rho_c(z) f_{b, \text{cosmo}} \Big(\frac{\mu}{\mu_e} \Big) \Big(\frac{GM_{500}}{2R_{500}} \Big), \\ h_{70} &= H_0/70 \text{ km s}^{-1} \text{ Mpc}^{-1}, \\ \text{and } \mathbb{P}(x) &= P_0 (c_{500} x)^{-\gamma} (1 + (c_{500} x)^{\alpha})^{-(\beta - \gamma)/\alpha}. \end{split} \tag{8}$$

Here, μ is the mean molecular weight; μ_e is the mean molecular weight per free electron; α_p corresponds to a modification of the standard self-similarity; $\alpha_p{}'(x)$ introduces a break in the self-similarity; c_{500} is the concentration factor; and α , β , and γ are the slopes of the pressure profile at $x \approx r_s$, $x \gg r_s$, and $x \ll r_s$, respectively, where $r_s = R_{500}/c_{500}$. For local (z < 0.2) massive $(M_{500} > 10^{14} M_{\odot})$ galaxy clusters,

For local (z < 0.2) massive ($M_{500} > 10^{14} M_{\odot}$) galaxy clusters, Arnaud et al. (2010, hereafter A10) considered a hybrid average profile of pressure, combining profiles from X-ray observations within 0.03–1 R_{500} and simulations in the 1–4 R_{500} region. For their best-fit estimate of c_{500} , the r_s of our sample galaxies are smaller than the angular resolution of the y-maps that we consider in our analysis. Therefore, by construction, we cannot constrain the slopes of the pressure profile independently. Thus, we freeze c_{500} , α , β , γ , and α_p at their empirically derived best-fitted values in A10 (1.177, 1.0510, 5.4905, 0.3081, and 0.12, respectively) and neglect the weak radial dependence $\alpha'_p(x)$ as it has a second-order effect (adopted in Greco et al. 2015 for the tSZ profile of $M_{\star} > 10^{11.3} M_{\odot}$ galaxies). We freeze μ at 0.59 and μ_e at 1.14, the values adopted by Nagai et al. (2007). We set the initial P_o as $8.403h_{70}^{-1.5}$ (best-fitted value in A10) and allow it to vary.

We use Markov Chain Monte Carlo calculations (Metropolis et al. 1953; Hastings 1970) to estimate the posterior probability distribution functions of $P_{\rm o}$, $A_{\rm 2h}$, and $y_{\rm zp}$, using the affine-invariant ensemble sampler algorithm implemented in emcee (Foreman-Mackey et al. 2013). We assume uniform priors on $0 \le P_{\rm o} \le 200$ and $0 \le A_{\rm 2h} \le 10$ and do not put any constraint on $y_{\rm zp}$. We assume the likelihood to be Gaussian. We run multiple emcee ensembles and keep on adding independent sets of chains until (i) the number of chains is larger than 50 times the integrated autocorrelation time, τ , of each parameter,

and (ii) the Gelman–Rubin convergence parameter reaches values within 0.9–1.1 (Gelman & Rubin 1992). We remove the first 2 \times $\tau_{\rm max}$ steps from the sampler to get rid of the burn-in phase. We consider the most likely values of the free parameters (i.e., values corresponding to the minimum χ^2) and the covariance matrices of their posterior probability distributions for the following calculations.

2.9. Thermal Energy

From the best-fit pressure profiles in Section 2.8 we calculate $Y_{R500}^{\rm sph}$, i.e., the thermal pressure of free electrons⁸ integrated within a spherical volume of radius R_{500} . Following convention, it is multiplied by $\sigma_{\rm T}/m_ec^2$ and divided by $D_A(z)^2$ in order to express it in units of the solid angle subtended by the spherical volume of consideration in the sky:

$$Y_{R500}^{\text{sph}} = (\sigma_{\text{T}}/m_e c^2) \int_0^{R_{500}} P_e(r) 4\pi r^2 dr / D_A(z)^2$$
 (9a)

$$\widetilde{Y}_{R500}^{\text{sph}} = \widetilde{Y}_{R500}^{\text{sph}} E(z)^{-2/3} (D_A(z)/500 \text{ Mpc})^2.$$
 (9b)

 $\tilde{Y}_{R500}^{\rm sph}$ takes into account different redshifts of galaxies, scales $Y_{R500}^{\rm sph}$ to z=0 through E(z), and normalizes $Y_{R500}^{\rm sph}$ to a fixed angular diameter distance of 500 Mpc.

2.10. Baryonic Mass and Baryon Fraction

We assume that the hot CGM, i.e., the ionized gas within R_{200} of the stacked galaxies in each mass bin, is at the virial temperature, $T_{\rm vir}$ ($\equiv T_{200}$). We estimate T_{200} from the virial mass and the virial radius (Equation (10b)). We estimate the density profiles from the best-fitted pressure profiles in Section 2.8 and calculate the mass of the hot circumgalactic gas using Equation (10a):

$$M_{\rm gas,200} = \int_0^{R_{\rm 200}} \mu_e m_p n_e(r) 4\pi r^2 dr,$$
 where $n_e(r) = P_e(r) k_{\rm B}^{-1} T_{\rm 200}^{-1},$ (10a)

$$T_{200} = \frac{\mu m_p G M_{200}}{2k_{\rm R} R_{200}}. (10b)$$

Here, m_p , n_e , and $k_{\rm B}$ are the rest mass of the proton, the number density of electrons, and Boltzmann's constant, respectively. Finally, we calculate the baryon fraction, $f_b = (M_\star + M_{\rm gas,200})/M_{\rm 200}$.

2.11. Null Test

For the null test, we create a mock catalog of galaxies in each patch of the sky, i.e., BN and D56. We construct a 2D random distribution spanning the range of R.A. and decl. of our sample and replace the true location (R.A., decl.) of the galaxies with values drawn from that distribution. Then, we repeat the stacking, aperture photometry, and error estimation of Compton-y for this mock catalog of galaxies.

3. Results and Discussion

In the following sections, we discuss the results derived from the CIB and Galactic dust-corrected, galaxy cluster and radio source-masked y-maps stacked using the third stacking method. We discuss the individual effects of the CIB, Galactic dust, galaxy clusters, and radio sources on stacking and compare the three stacking methods in Appendix A.

3.1. Best-fit Model

In Figure 5, we show the results of stacking (top left panel) and pressure modeling for the $M_{\star} = 10^{11.0-11.3} M_{\odot}$ mass bin. A_{2h} is greater than 1, and y_{zp} is consistent with zero within a 1σ uncertainty (top right panel), implying a significant contribution of the "two-halo" term and a negligible contribution of the zero-point offset. A_{2h} and y_{zp} are anticorrelated as expected for a given tSZ background. In the bottom left panel, we show the differential radial profile of Compton-y extracted from the stacked y-map (black circles with error bars) and the profile calculated from the best-fitted pressure model (red curve). The "one-halo" term (blue dashed-dotted curve) contributes at a small radius, while the tSZ background (dashed green curve) dominates at a large radius. The excess in the data as compared to the tSZ background in the innermost radial bin indicates the detection of the tSZ effect in the CGM of $M_{\star} = 10^{11.0-11.3} M_{\odot}$ galaxies. We show the results for other mass bins in Appendix B.

3.2. Dependence on Stellar Mass

In Figure 6 (left panel) we show the best-fit thermal pressure of electrons integrated within a spherical volume as a function of the stellar mass of the galaxies. Qualitatively, the thermal energy increases with stellar mass and flattens at $M_{\star} > 10^{11} M_{\odot}$.

We compare our measurements with the predictions from cosmological zoom-in simulations EAGLE (4262 galaxies) and IllustrisTNG (5768 galaxies; Kim et al. 2022, hereafter K22). While EAGLE and IllustrisTNG have different feedback prescriptions, their predicted median $\tilde{Y}_{R500}^{\rm sph}$ are consistent with each other. Our measurements for $M_{\star} < 10^{11} M_{\odot}$ including the upper limits are consistent with the median of the simulations. Our measurements for $M_{\star} > 10^{11} M_{\odot}$ are smaller than the median, but are fairly consistent within the scatter ("×" and "+" symbols).

The simulations in K22 were tuned to reproduce the results of Planck Collaboration et al. (2013) within $5 \times R_{500}$ of $M_{\star} > 10^{11.3} M_{\odot}$ LBGs (galaxies without any brighter neighbor within 1 Mpc). LBGs have a different luminosity function than the whole population of galaxies. But we do not have any such preference. Therefore, the discrepancy between K22's and our results at $M_{\star} = 10^{11.0-11.3} M_{\odot}$ could be due to sample selection. It should be noted that the galaxies in K22 were at z=0, whereas our $M_{\star} > 10^{11} M_{\odot}$ galaxy sample is at $z\approx 0.28$ (Table 1). Also, the star-forming galaxies have larger $\tilde{Y}_{R500}^{\rm sph}$ than the quiescent galaxies in K22. Therefore, the discrepancy could be due to any redshift evolution, and/or our galaxy sample being dominated by quiescent galaxies. We will test these possibilities in future work.

3.3. Self-similarity

In the right panel of Figure 6 we show the volume-integrated thermal pressure of electrons as a function of the virial mass (M_{500}) of galaxies. A10 introduced a modification to the self-similarity to fit the X-ray observations of $M_{500} > 10^{14} M_{\odot}$ halos:

⁸ For a fully ionized monatomic ideal gas, the thermal energy density is $\left(\frac{3\mu_e}{2\mu}\right)P_e\sim 2.9P_e$. The self-similarity (or lack thereof) of $Y_{R500}^{\rm sph}$ is not affected by the proportionality factor. Because the goal of this paper is to study $Y_{R500}^{\rm sph}$ as a function of mass, we do not explicitly discuss the thermal energy further.

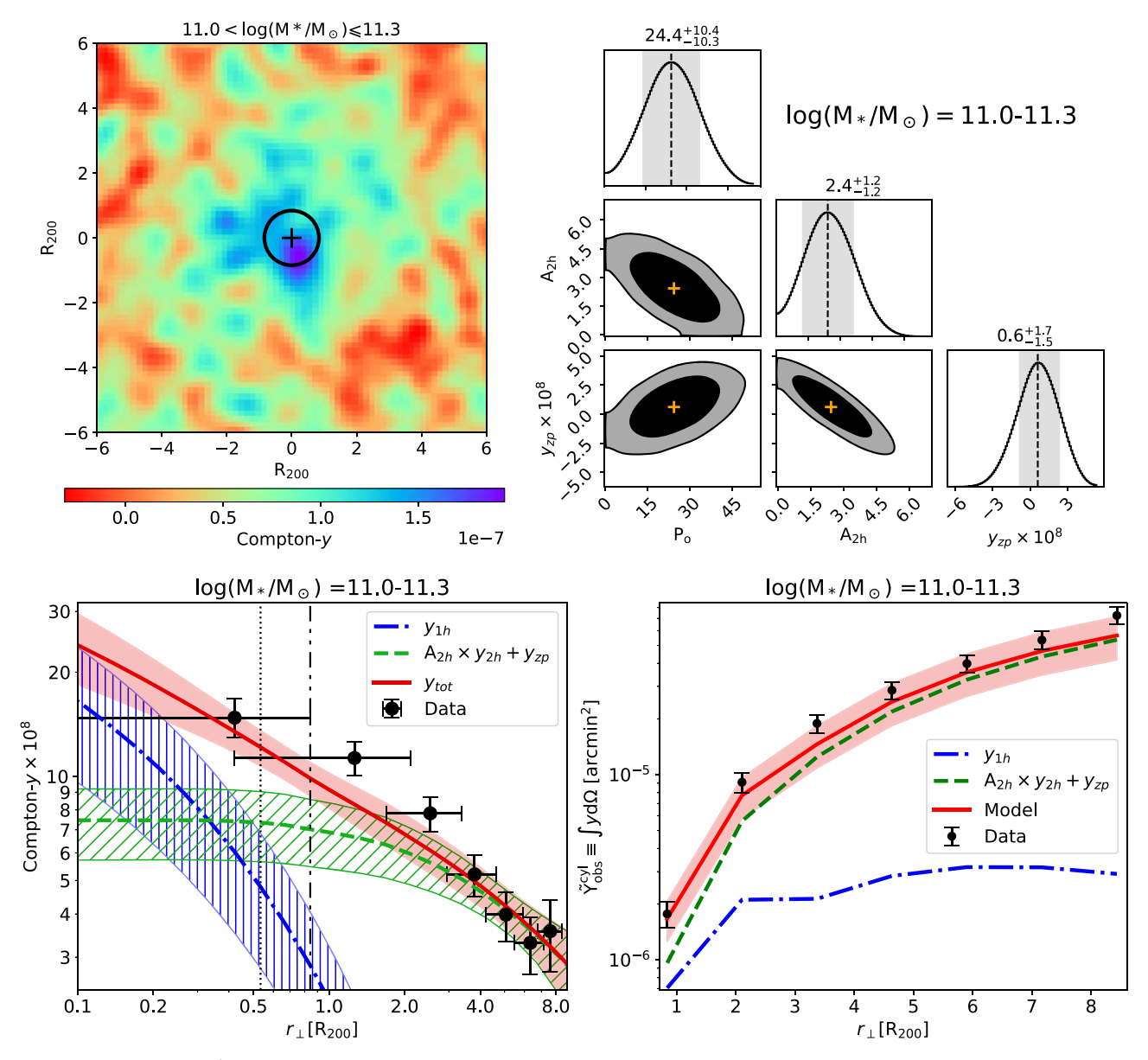


Figure 5. Results for the $\log(M_*/M_\odot) = 11.0-11.3$ mass bin. Top left: CIB and Galactic dust-corrected, galaxy cluster and radio source-masked Compton-y map stacked using method (iii) (fixed f_{200}). The center of the stacked galaxies (i.e., the central pixel) is marked with a plus ("+") sign. The Gaussian beam (FWHM of 2,4) is shown as a circle at the center of the map. The color bar is shown below the map. Top right: Posterior probability distributions of the amplitude of the thermal pressure profile, P_o ; the amplitude of y_{2h} , A_{2h} ; and the zero-point offset y_{zp} , obtained by fitting the GNFW pressure model to our tSZ measurements. The vertical dashed lines and the shaded regions in the diagonal plots correspond to the most likely value and 68% confidence interval of the marginalized distribution of the free parameters; the values are mentioned in the respective headings. The most likely values are marked with "+" in the contour plots. The contours correspond to 68% and 95% confidence intervals. Bottom left: Differential radial profile of Compton-y. The black circles with error bars are extracted from the map shown above (see Section 2.5). The dashed-dotted-dotted vertical line denotes the FWHM of the beam (2,4). By construction, the width of each annulus is the same as the beam size, shown with the error bars along the x-axis. The error bars along the y-axis denote 68% confidence intervals. The dotted vertical line is drawn at R_{500} . The dashed-dotted blue curve and the dashed green curve are the best-fit "one-halo" term y_{1h} and tSZ background ($A_{2h}y_{2h} + y_{zp}$), respectively, with the hatched area around them corresponding to the 1σ uncertainty. The solid red curve and the shaded area around it are the best-fit model with 1σ uncertainties. Bottom right: Cumulative radial profile of Compton-y, i.e., $\int y d\Omega$, normalized at an angular diameter distance of 500 Mpc. The black circles with error bars are extracted from the model and its 1σ uncertainties, best fitted to the di

 $\tilde{Y}_{R500}^{\rm sph} \propto M_{500}^{5/3+\alpha_p}$ with $\alpha_p = 0.12$ (see Section 2.8). We extrapolate this relation to lower mass and compare it (dotted blue line) with our results (black circles).

blue line) with our results (black circles). With the expectation that M_{500} and $\tilde{Y}_{R500}^{\rm sph}$ follow a power-law relation, $\tilde{Y}_{R500}^{\rm sph} = Y_{\rm norm} \times M_{500}^{\Gamma}$, we fit a straight line to $\ln(M_{500})$ and $\ln(\tilde{Y}_{R500}^{\rm sph})$ using the Python package linmix based on the

hierarchical Bayesian model of Kelly (2007). M_{500} and $\tilde{Y}_{R500}^{\rm sph}$ are assumed to be drawn from a 2D lognormal distribution

 $[\]mathcal{N}_2(\mu, \Sigma)$ with the mean $\mu = (\xi, \eta)$, which are the unobserved true values of $\ln(M_{500})$ and $\ln(\tilde{Y}_{R500}^{\rm sph})$, and the covariance matrix Σ containing the measured errors of $\ln(M_{500})$ and $\ln(\tilde{Y}_{R500}^{\rm sph})$. The variables ξ and η are connected through $P(\eta|\xi) = \mathcal{N}(\alpha + \beta\xi, \sigma^2)$, where the regression parameters α , β , and σ^2 are the intercept, slope, and Gaussian intrinsic scatter of η

https://github.com/jmeyers314/linmix

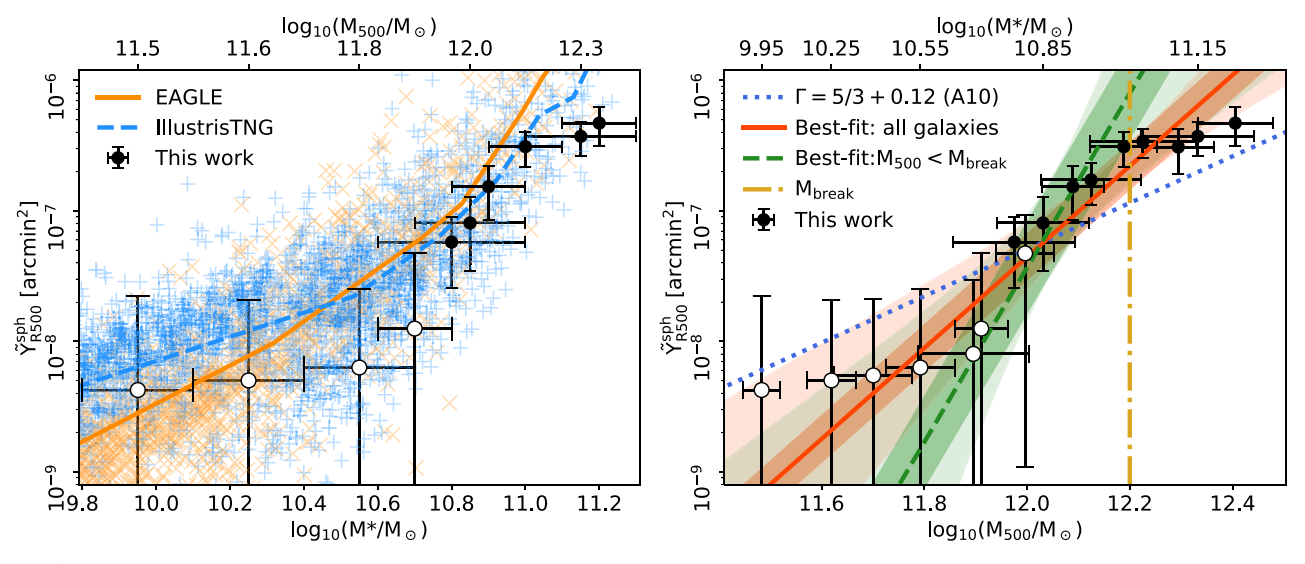


Figure 6. $\tilde{Y}_{R500}^{\rm sph}$, a measure of the thermal energy within R_{500} , as a function of the stellar mass M_{\star} (left) and halo mass M_{500} (right). The upper x-axes have been labeled with the corresponding M_{500} (left) and M_{\star} (right). The error bars in the y-axes are 1σ uncertainties. Our measurements of $\tilde{Y}_{R500}^{\rm sph}$ constrained at more/less than 90% confidence are plotted as filled/unfilled black circles. Left: The error bars in the x-axes correspond to the range of M_{\star} in the mass bin of consideration. We have plotted a subset of the results (Table 1) to help us visualize the pattern. The orange "×" and blue "+" symbols are the $\tilde{Y}_{R500}^{\rm sph}$ predicted from cosmological zoom-in simulations EAGLE and IllustrisTNG, respectively (Kim et al. 2022), with solid orange and dashed blue curves showing the median. Right: The error bars in the x-axes correspond to the 1σ scatter in M_{500} . The dotted blue line is the best-fit result of $\tilde{Y}_{R500}^{\rm sph} \propto M_{500}^{5/3+\alpha_p}$ for $M_{500} > 10^{14} M_{\odot}$ halos (Arnaud et al. 2010; see Section 2.8), extrapolated to lower mass. The solid red and dashed green curves are the best-fit results for all galaxies and $M_{500} \leq M_{\rm break}$ galaxies, respectively. $M_{\rm break}$ is marked with a vertical dashed–dotted yellow line. The dark and light shaded areas denote the intrinsic and total scatter in the regression, respectively. See Sections 3.2 and 3.3 for details.

around the regression line, respectively. The priors on α , β , and σ^2 are uniform.

The best-fit value of β , i.e., the true value of Γ , is $3.27^{+0.91}_{-0.69} \equiv 5/3 + 1.60^{+0.91}_{-0.69}$ (68% confidence interval; solid red line in Figure 6, right panel). It implies that our sample galaxies deviate from the self-similarity relation by $\approx 2.3\sigma$. The deviation from self-similarity is stronger than the α_p of A10, i.e., $1.60^{+0.91}_{-0.69} > 0.12$. The largest possible value of the second-order effect, $\alpha_p{'}(r/R_{500})$, which we have ignored in our analysis (see Section 2.8), was 0.10 in A10. The equivalent $\alpha_p{'}$ in our case is $1.48^{+0.91}_{-0.69}$. Therefore, our sample not only deviate from self-similarity but also deviate more than their massive counterparts in A10. Our finding of a steeper $\tilde{Y}^{\rm sph}_{R500} - M_{500}$ relation is consistent with the best-fit model for $\gtrsim 25,000$ simulated halos in the mass range of $10^{12}M_{\odot} < M_{500} < 5 \times 10^{13}M_{\odot}$ in IllustrisTNG (Pop et al. 2022).

It should be noted that $\tilde{Y}_{R500}^{\rm sph}$ is practically constant at $M_{500} > 10^{12.2} M_{\odot}$ (see the values of $\tilde{Y}_{R500}^{\rm sph}$ in the last two rows of $\Delta M_{\star} = 0.3$ dex and 0.2 dex in Table 1). To test if this flattening affects the best-fitted $\tilde{Y}_{R500}^{\rm sph} - M_{500}$ relation, we fit the $M_{500} \leq 10^{12.2} M_{\odot}$ halos, and obtain $\Gamma = 5.49_{-1.95}^{+4.57}$ (dashed green line in Figure 6, right panel), which is larger than the slope for self-similarity, the slope of A10, and the slope we obtain for all our galaxies: $3.27_{-0.69}^{+0.91}$. That means the overall $\tilde{Y}_{R500}^{\rm sph} - M_{500}$ relation of our sample might follow a broken power law with $M_{\rm break} \approx 10^{12.2} M_{\odot}$, where the relation is weaker than the self-similarity above $M_{\rm break}$ but is stronger than the self-similarity below $M_{\rm break}$. It has not been predicted or observed before.

Our results for the global fit and the fit for $M_{500} \leq 10^{12.2} M_{\odot}$ galaxies are qualitatively similar: they show a deficit of the tSZ effect at a given stellar (and halo) mass as compared to the self-similarity. It indicates two possibilities

regarding galactic outflows: (1) too strong feedback, where the galactic outflow spews ionized gas in the CGM outside R_{500} , or (2) too weak feedback, i.e., feedback is not strong enough to prevent cooling and eventual precipitation of the halo gas to the galactic disk. Distinguishing between these options and identifying the actual physical scenario is beyond the scope of our paper. It will be part of our future endeavors.

The interpretation of our result for $M_{500} > M_{\text{break}}$ galaxies depends on which side of the mass is considered the point of reference. If we consider M_{break} as the reference, the flattening of $\tilde{Y}_{R500}^{\text{sph}}$ implies a deficit of $\tilde{Y}_{R500}^{\text{sph}}$ in the CGM of the most massive galaxies in our sample as compared to the selfsimilarity relation (and that of A10). In that case, the interpretation would be similar to that discussed in the previous paragraph. If we consider the most massive galaxies in our sample as a reference, the flattening of $\tilde{Y}_{R500}^{\rm sph}$ implies an excess of $\tilde{Y}_{R500}^{\rm sph}$ in the CGM of galaxies above $M_{\rm break}$. It indicates a nonnegligible contribution of galactic feedback within R_{500} that keeps the CGM ionized but does not throw the gas outside the halo. However, there are only four data points at $M_{500} > M_{\text{break}}$, and they span only 0.2 dex of virial mass. Also, only 5% of our galaxy sample are more massive than M_{break} . Therefore, we do not comment further on $M_{500} > M_{\text{break}}$ galaxies to avoid overinterpretation.

3.4. Baryon Budget

In Figure 7, we show the baryon fraction f_b as a function of the stellar mass. We compare our measurements with the predictions from cosmological zoom-in simulations EAGLE (3544 galaxies) and IllustrisTNG (5344 galaxies; Davies et al. 2020), and with previous measurements based on X-ray observations. Finally, we discuss the implications of the variation of the baryon fraction with stellar mass in our sample.

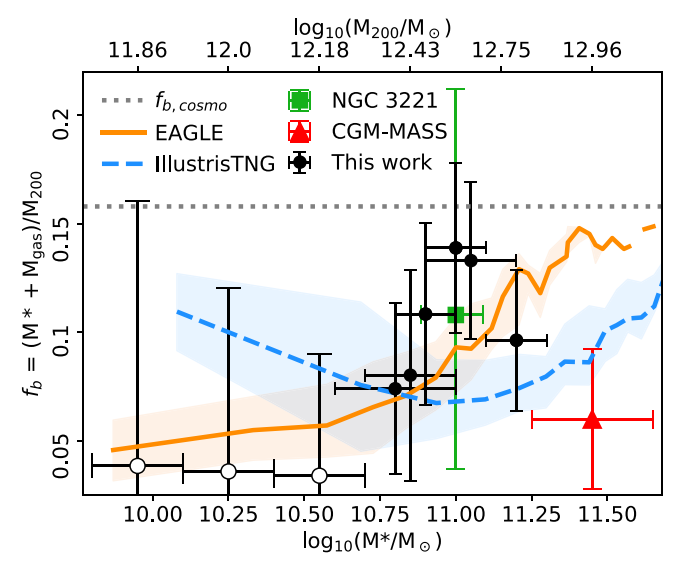


Figure 7. The baryon fraction, f_b , as a function of the stellar mass. The upper x-axis has been labeled with the corresponding M_{200} . Our measurements constrained at more (less) than 90% confidence are plotted as filled (unfilled) black circles. Note that we have plotted a subset of the results (Table 1) to help us visualize the pattern. The error bars in the x-axes correspond to the range of M_{\star} in the mass bin of consideration. The green square and the red triangle are based on the X-ray emission measurement of NGC 3221 (Das et al. 2019b, 2020) and of six galaxies in the CGM-MASS survey (Li et al. 2018), respectively. The solid orange and dashed blue curves are the median predictions from EAGLE and IllustrisTNG, with the shaded regions showing 1σ scatter (Davies et al. 2020). The horizontal dotted gray line corresponds to the cosmological baryon fraction (Planck Collaboration et al. 2016)

The X-ray emission—based measurement of NGC 3221, the only L^* galaxy other than the Milky Way with a detected CGM (green square; Das et al. 2019b, 2020), is consistent with our results. The measurements for more massive super- L^* galaxies in X-ray emission (red triangle; Li et al. 2018) are also in line with our findings. Instead of assuming an SHMR, the virial masses of these individual galaxies have been directly measured from the velocity dispersion of the neutral gas in these galaxies. The measurement uncertainty in the virial mass is the largest source of uncertainty in f_b of these individual galaxies. The medians of the f_b distributions predicted in the simulations (solid orange and dashed blue curves, Figure 7) are not consistent with our measurements, but we cannot rule these predictions out modulo the scatter around the median and the uncertainties in our measurements.

In previous studies on galaxy groups and clusters based on the tSZ effect and X-ray emission, f_b has been found to decrease with decreasing halo mass (e.g., Lim et al. 2018). However, we find that the trend does not continue in low-mass halos. Starting from the largest stellar mass in Figure 7, f_b increases with decreasing stellar mass, reaches its peak, becomes consistent with the cosmological f_b at $M_{\star}=10^{10.9-11.2}M_{\odot}$, and falls off at lower stellar mass. It is arguably the first time that the baryon fraction has been found to show such a nonmonotonic behavior with stellar (and virial) mass in observational data. This "inversion," i.e., increasing f_b with decreasing stellar mass, has been predicted in IllustrisTNG simulations (Davies et al. 2020; blue dashed curve, Figure 7), although the "inversion" in the simulation occurs at a different stellar mass from our measurements.

It should be noted that we assume the gas to be at the virial temperature. The X-ray emission measurements of

 $M_{\star} > 10^{10.9} M_{\odot}$ galaxies (Li et al. 2018; Das et al. 2020) are consistent with that, but it might not be true for lower-mass galaxies. While the exact mass of subvirial phases in the CGM probed in UV absorption lines is extremely sensitive to the conditions in ionization modeling, the prevalence of those lines indicates that the volume-averaged temperatures of these halos might not be as high as their corresponding virial temperatures. A lower temperature would increase the mass of the CGM calculated from the tSZ effect, thereby increasing f_b in $M_{\star} < 10^{10.9} M_{\odot}$ halos.

In galaxy groups and clusters, as active galactic nucleus (AGN) feedback is the dominant mechanism of outflows, decreasing f_b with decreasing halo mass (e.g., Lim et al. 2018) indicates a higher strength of the AGN feedback relative to gravitation in low-mass groups. The halo mass of our sample is where the stellar feedback could become more influential than the AGN feedback (e.g., Harrison 2017). Therefore, the "inversion" in f_b from $M_\star=10^{11.6}M_\odot$ to $10^{10.9}M_\odot$ galaxies in Figure 7 might be the scenario where stellar feedback enriches the CGM and prevents overcooling but unlike AGN feedback, it is not strong enough to throw the gas outside R_{200} . In $M_{\star} < 10^{10.9} M_{\odot}$ galaxies, given the ubiquitous presence of a cool CGM, we cannot conclusively comment on the baryon sufficiency and the interplay between feedback and cooling. It would require simulations focused on the large-scale impact of stellar feedback and observations in X-ray and kinetic SZ (kSZ) effect¹⁰ (e.g., as done in Amodeo et al. 2021; Schaan et al. 2021) to constrain these speculations.

4. Conclusion, Summary, and Future Directions

In this paper, we have looked for the tSZ effect in the CGM of WISE × SuperCOSMOS galaxies with $M_{\star}=10^{9.8-11.3}M_{\odot}$ using Compton-y maps from ACT + Planck data. We have studied the effects of dust, galaxy clusters, and radio sources on the stacked y-maps and corrected them. We have considered three methods of stacking, and two methods of aperture photometry, and zeroed in on the most complete and informative one. We have taken into account beam smearing, the "two-halo" term, and any zero-point offset. Below, we summarize our science results:

- 1. We have been able to constrain the tSZ effect in the CGM of $M_{\star} = 10^{10.6-11.3} M_{\odot}$ galaxies by modeling the thermal pressure with a GNFW profile. There is also indirect evidence of the tSZ effect in the $M_{\star} < 10^{10.6} M_{\odot}$ galaxies before correcting for the CIB (Figure A1, top row), but we cannot quantify the signal after correcting for the CIB.
- we cannot quantify the signal after correcting for the CIB.

 2. The dependence of $\tilde{Y}_{R500}^{\rm sph}$ (a measure of the thermal energy within R_{500}) on the virial mass M_{500} is $>2\sigma$ stronger than the self-similarity relation and the deviation from the same observed in higher-mass halos in literature.

 3. Galaxies in the $10^{10.9-11.2}M_{\odot}$ range of stellar mass could
- 3. Galaxies in the $10^{10.9-11.2}M_{\odot}$ range of stellar mass could be baryon-sufficient. The baryon fraction of the galaxies exhibits a nonmonotonic trend with stellar mass, implying a complex interplay of the gravitational potential and galactic outflow. The nonmonotonic trend has not been predicted before, indicating an insufficient treatment of the large-scale effect of galactic feedback in low-mass galaxies in simulations.

 $[\]overline{^{10}}$ A measure of n_e from the CMB power spectrum, without any temperature dependence.

Upcoming telescopes, e.g., Simons Observatory and CMB-S4, will improve the quality of the SZ signal with increased sky coverage, frequency coverage, sensitivity, and angular resolution. Ongoing and future galaxy surveys, e.g., by the Dark Energy Spectroscopic Instrument (DESI) and Vera C. Rubin Observatory, will increase the sample size of galaxies. This will allow us to measure the tSZ effect as well as the kSZ effect in low-mass galaxies and constrain the density and pressure profiles independently, leading to a better understanding of the effect of galactic feedback on the CGM.

Acknowledgments

We thank the anonymous referee for constructive feedback. We thank Dr. Vinu Vikram, Dr. Junhan Kim, and Dr. Jonathan Davies for sharing the data of their Vikram et al. (2017), Kim et al. (2022), and Davies et al. (2020) papers, respectively. S.D. acknowledges support from the Presidential Graduate Fellowship of The Ohio State University and the KIPAC Fellowship of the Kavli Institute for Particle Astrophysics and Cosmology, Stanford University. Y.-K.C. acknowledges the support of the National Science and Technology Council of Taiwan through

grant NSTC 111-2112-M-001-090-MY3. S.M. is grateful for support from NASA through ADAP grant 80NSSC22K1121. This research has made use of NASA's Astrophysics Data System Bibliographic Services.

Facilities: WISE, Planck, VLA.

Software: Astropy (Astropy Collaboration & Astropy Project Contributors 2022), corner (Foreman-Mackey 2016), emcee (Foreman-Mackey et al. 2013), Halotools (Hearin et al. 2016), Jupyter (Kluyver et al. 2016), Matplotlib (Hunter 2007), NumPy (Harris et al. 2020), pandas (The pandas development team 2020), pixell (Naess et al. 2021), Python math (Van Rossum 2020), SciPy (Gommers et al. 2022).

Appendix A Proof of Concept and Techniques

A.1. Effect of Thermal Dust

In this section, we discuss how the CIB and Galactic dust affect the stacking results.

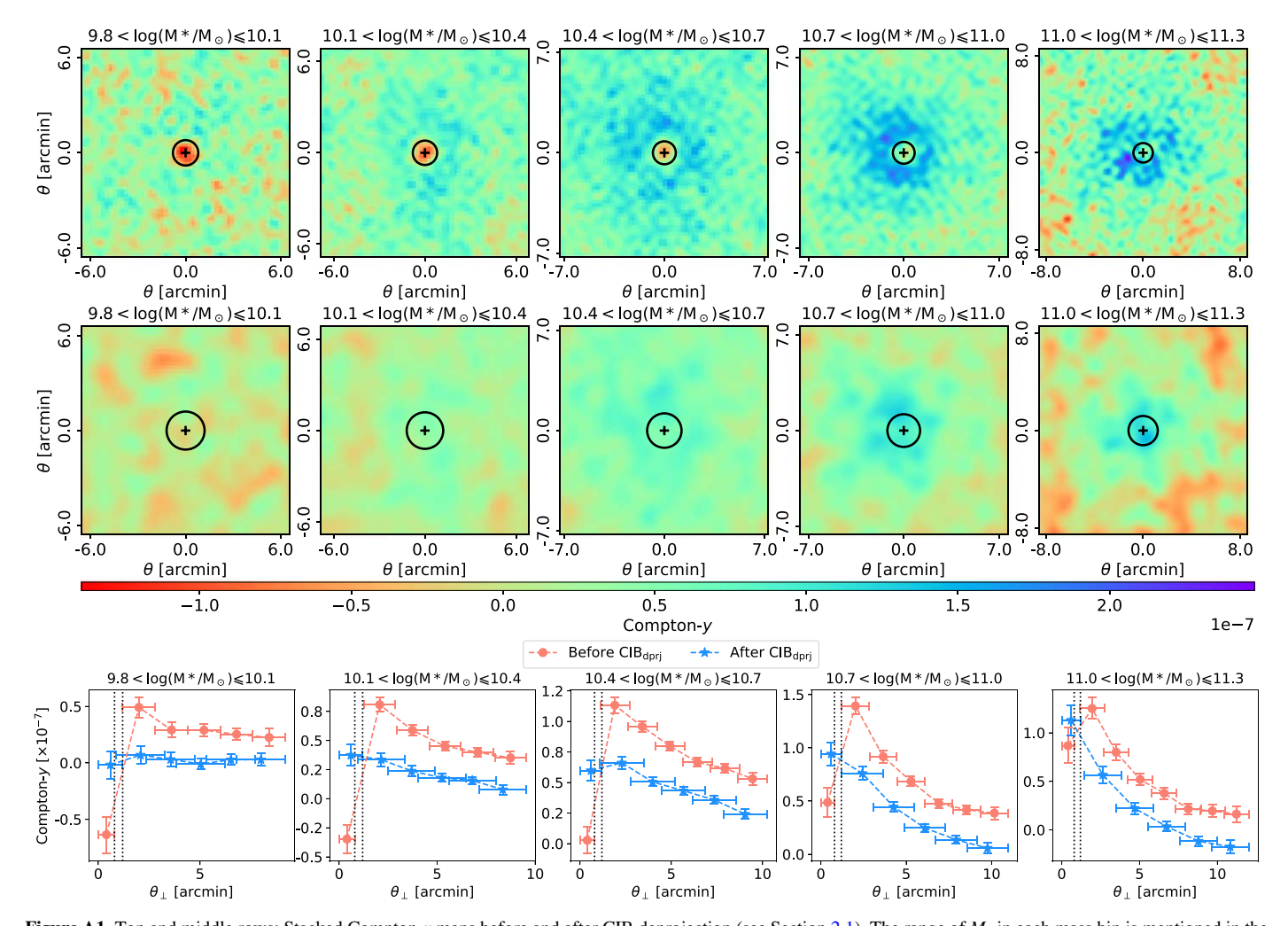


Figure A1. Top and middle rows: Stacked Compton-y maps before and after CIB deprojection (see Section 2.1). The range of M_{\star} in each mass bin is mentioned in the heading of each map. The center of the stacked galaxies (i.e., the central pixel) is marked with a plus ("+") sign. The Gaussian beam with an FWHM of 1!6 and 2!4 before and after the CIB deprojection, respectively, is shown as a circle at the center of each map. The color bar is shown at the bottom. Bottom row: Differential radial profiles of the stacked Compton-y maps with 1σ error before and after the CIB deprojection. The width of each annulus is the same as the FWHM of the Gaussian beam, shown with the error bars along the x-axis.

A.1.1. CIB

We show the stacked y-maps and the corresponding differential radial profiles before and after CIB deprojection in Figure A1. The y-value in the central region of the maps before CIB deprojection is suppressed (top row). It is also reflected by the radial profiles (red circles, bottom row), where the y-value in the innermost radial bin is smaller than the y-values in most (if not all) of the outer radial bins. Because the thermal dust of the galaxies has a different SED from that of the tSZ effect, the dust emission could manifest as a dearth of Compton-y. This effect becomes stronger as the stellar mass decreases, to the extent of the innermost radial bin falling to negative Comptony, which is unphysical. It attests to the fact that less massive galaxies are generally dustier (e.g., Cortese et al. 2012). Also, the y-values in the outer radial bins are enhanced due to the thermal dust emission by the CIB, which mimics the tSZ signal. Both of these effects are corrected in the CIBdeprojected maps (middle row) and the corresponding radial

profiles (blue stars, bottom row). In the following sections, we consider the CIB-corrected results only.

A.1.2. Galactic Dust

We show the stacked, CIB-deprojected y-maps and the corresponding differential radial profiles before and after correcting for Galactic dust in Figure A2. The Compton-y maps after applying the cut in $N(\text{H I})_{\text{Gal}}$ are systematically brighter than those before applying the cut (middle versus top row). The correction factor is roughly constant at small angular separation ($\theta < 5'$), and it increases at larger angular separation. It leads to a flatter radial profile of Compton-y, effectively visible in the $10.7 < \log(M_{\star}/M_{\odot}) \le 11.3$ bins (red circles versus blue stars, bottom row). It also shows that the negative values of Compton-y at large angular separation ($\theta > 8'$) in the most massive ($11.0 < \log(M_{\star}/M_{\odot}) \le 11.3$) bin are due to the residual effect of Galactic dust even after the CIB correction. In the following sections, we consider the results corrected for the CIB as well as for Galactic dust.

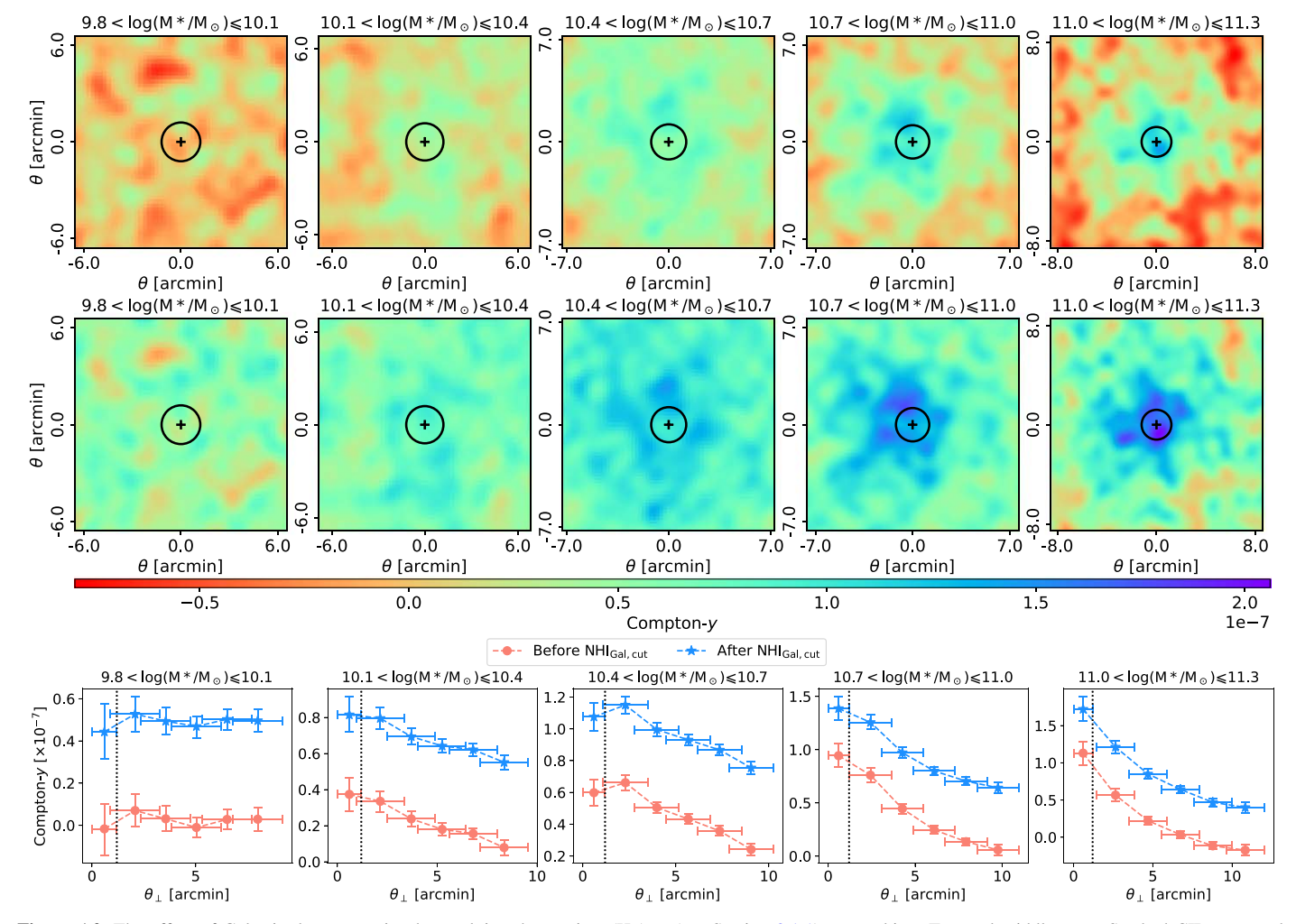


Figure A2. The effect of Galactic dust correction by applying the cut in $N(\text{H I})_{\text{Gal}}$ (see Section 2.1.1) on stacking. Top and middle rows: Stacked CIB-corrected Compton-y maps before and after the cut. The range of M_{\star} in each mass bin is mentioned in the heading of each map. The center of the stacked galaxies (i.e., the central pixel) is marked with a plus ("+") sign. The Gaussian beam (FWHM of 2.4) is shown as a circle at the center of each map. The color bar is shown at the bottom. Bottom row: Differential radial profiles of the stacked Compton-y maps with 1σ error before and after the cut. The width of each annulus is the same as the FWHM of the Gaussian beam, shown with the error bars along the x-axis.

A.2. Effect of Masking

In this section, we discuss how galaxy clusters and compact radio sources affect the stacking results.

A.2.1. Galaxy Clusters

In Figure A3, we show the stacked y-maps and the corresponding differential radial profiles before and after excluding galaxy clusters. The Compton-y values are significantly larger in the presence of galaxy clusters, reflected by

the stark differences between the stacked *y*-maps (top and middle rows). This difference could be due to the tSZ emission from the ICM of the galaxy clusters. However, the clusters not only enhance the overall *y*-values but also steepen the radial profiles (red circles, bottom row), which would effectively lead to an overestimation of the tSZ signal. This contamination is corrected for in the masked profiles (blue stars, bottom row). In the following section, we consider the results masked for galaxy clusters.

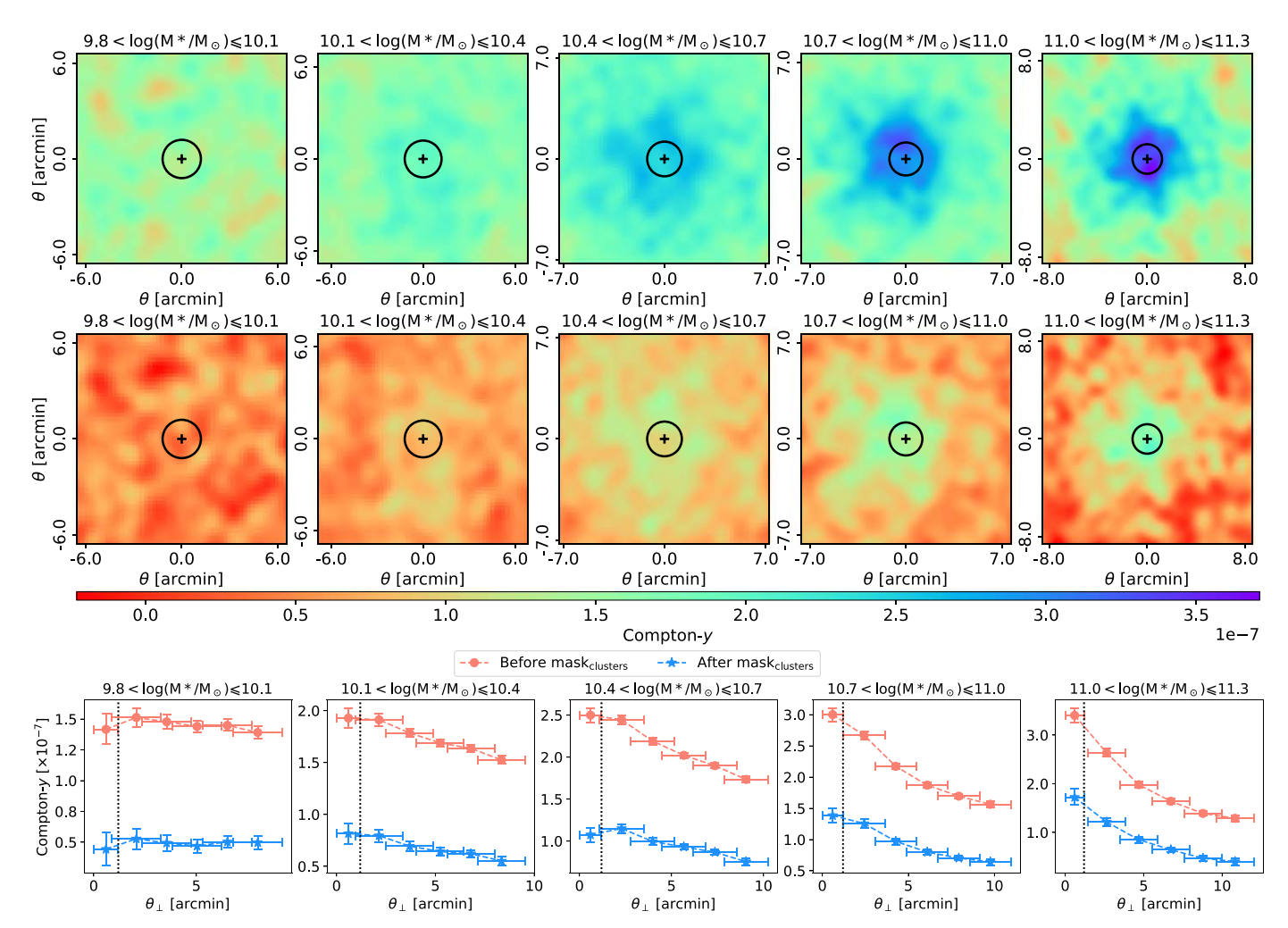


Figure A3. The effect of masking galaxy clusters (see Section 2.3.1) on stacking. Top and middle rows: Stacked CIB and Galactic dust-corrected Compton-y maps before and after masking. The range of M_{\star} in each mass bin is mentioned in the heading of each map. The center of the stacked galaxies (i.e., the central pixel) is marked with a plus ("+") sign. The Gaussian beam (FWHM of 2'.4) is shown as a circle at the center of each map. The color bar is shown at the bottom. Bottom row: Differential radial profiles of the stacked Compton-y maps with 1σ error before and after masking. The width of each annulus is the same as the FWHM of the Gaussian beam, shown with the error bars along the x-axis.

A.2.2. Radio Sources

In Figure A4, we show the stacked y-maps and the corresponding differential radial profiles before and after removing radio sources from the WISE × SCOSPZ galaxy sample as well as from the y-map. Overall, the stacked y-maps are brighter after removing the radio sources (top and middle rows). Like the thermal dust, the compact radio sources, which include both stars and galaxies, have a different SED from that of the tSZ effect. Thus, the emission from these sources could manifest a deficiency of Compton-y. However, this effect is not uniform in all stellar mass bins or at all angular separations. In $\log(M_{\star}/M_{\odot}) \leq 10.4$ galaxies,

the *y*-values are systematically higher after masking the radio sources (red circles versus blue stars, bottom row). Thus, it increases the zero-point offset but does not affect the tSZ signal as such. In $\log(M_{\star}/M_{\odot}) > 10.4$ galaxies, the *y*-values at the innermost radial bins are practically unchanged, while the *y*-values in the outer bins are higher after masking the radio sources, thus flattening the radial profiles. Therefore, if the radio sources are not removed, the background would be underestimated and hence the tSZ signal would be overestimated. This is corrected in the masked profiles. In the main text, we discuss the results masked for galaxy clusters as well as for radio sources.

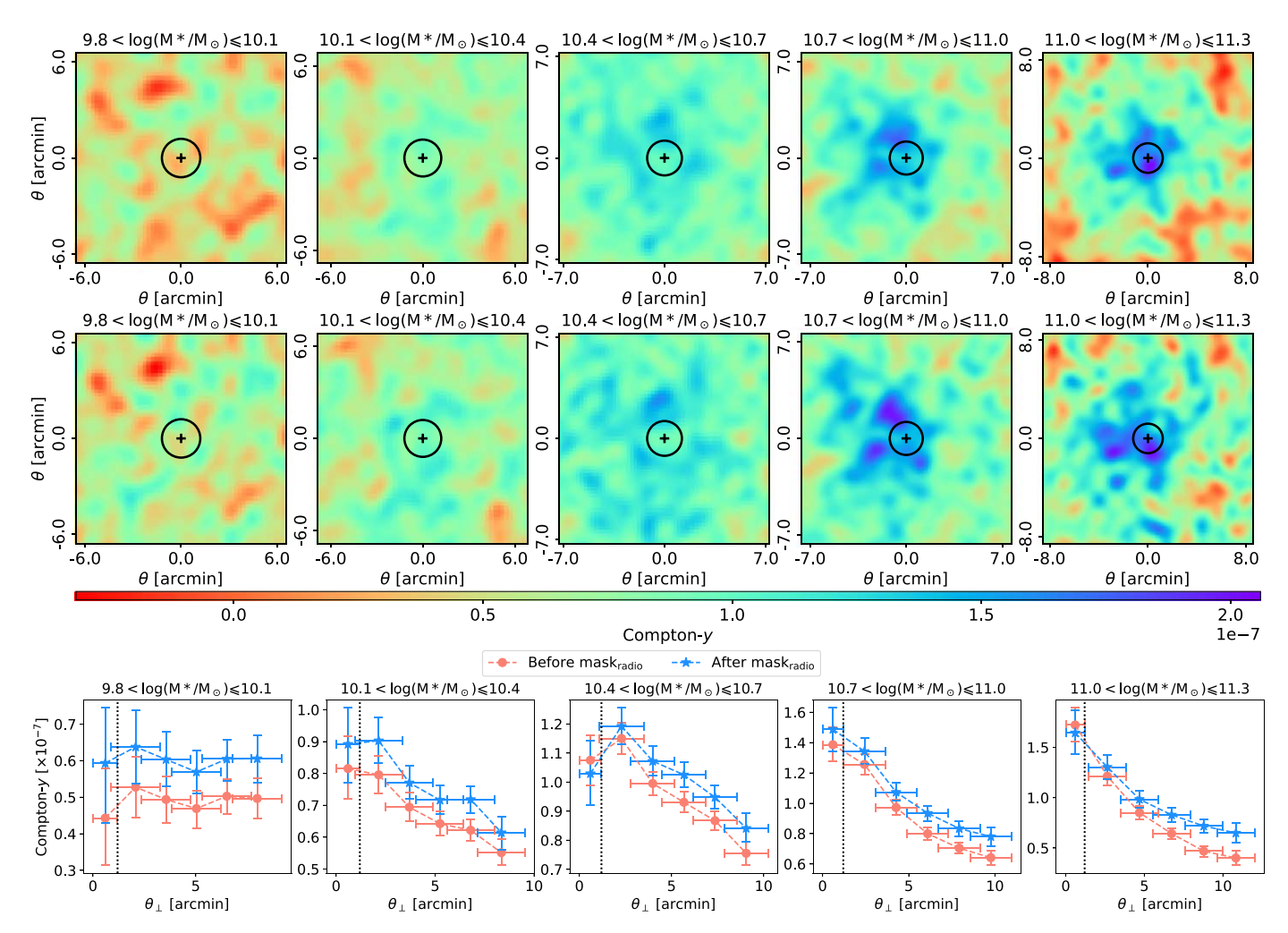


Figure A4. The effect of masking radio sources (see Section 2.3.2) on stacking. Top and middle rows: Stacked CIB and Galactic dust-corrected, galaxy cluster—masked Compton-y maps before and after masking. The range of M_{\star} in each mass bin is mentioned in the heading of each map. The center of the stacked galaxies (i.e., the central pixel) is marked with a plus ("+") sign. The Gaussian beam (FWHM of 2'.4) is shown as a circle at the center of each map. The color bar is shown at the bottom. Bottom row: Differential radial profiles of the stacked Compton-y maps with 1σ error before and after masking. The width of each annulus is the same as the FWHM of the Gaussian beam, shown with the error bars along the x-axis.

A.3. Comparison among Stacking Methods

We show the CIB and Galactic dust-corrected, galaxy cluster and radio source-masked y-maps stacked using the three stacking methods in Figure A5 (top three rows). The differences among the three stacking methods in the 2D spatial distribution of Compton-y in the maps are visible. We also show the corresponding differential and cumulative radial profiles in the bottom row of Figure A5. The units of galactocentric distance in these radial profiles are the

median θ_{200} , median R_{200} , and R_{200} for stacking methods (i) (fixed θ_{\perp}), (ii) (fixed r_{\perp}), and (iii) (fixed f_{200}), respectively. The radial profiles for the second and third stacking methods are consistent with each other (red crosses and orange circles), but the profiles for the first stacking method are different (crimson stars). In the differential profiles of Compton-y, the differences among the stacking methods are not uniform in all mass bins or at all radii. In the two lowest-mass bins, the y-values are noise-dominated, and the differences among the stacking methods in

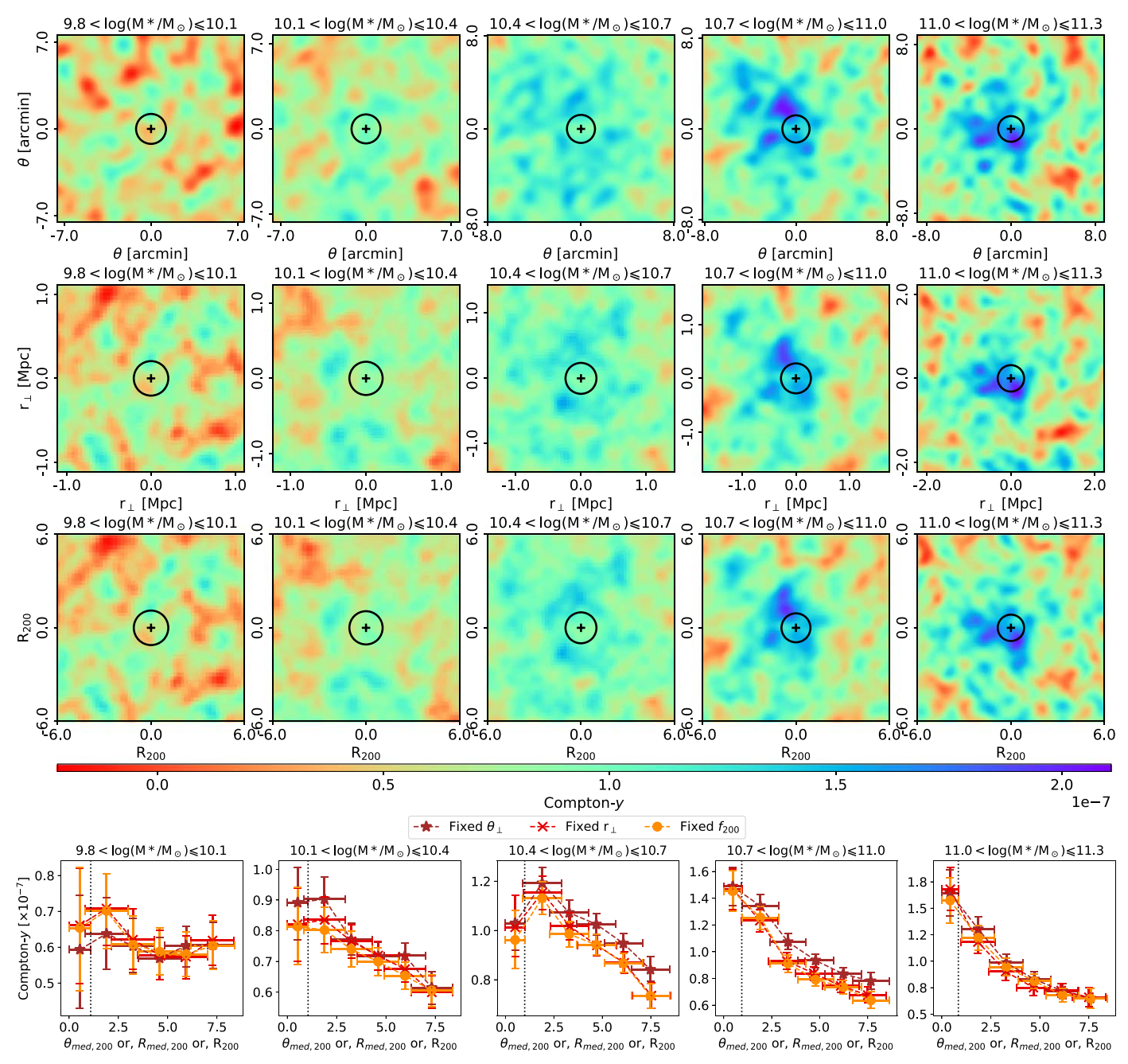


Figure A5. Top three rows: Compton-y maps stacked using methods (i) (fixed θ_{\perp} , top), (ii) (fixed r_{\perp} , middle), and (iii) (fixed f_{200} , bottom). The sizes of the maps are $6 \times \theta_{\text{med},200}$, $6 \times R_{\text{med},200}$, and $6 \times R_{200}$. The range of M_{\star} in each mass bin is mentioned in the heading of each map. The center of the stacked galaxies (i.e., the central pixel) is marked with a plus ("+") sign. The Gaussian beam (FWHM of 2',4) is shown as a circle at the center of each map. The color bar is shown below the third row. Bottom row: Comparison of the differential radial profiles of Compton-y among the three stacking methods. The range of M_{\star} in each mass bin is mentioned in the heading of each panel. The units of galactocentric distance are $\theta_{\text{med},200}$, $R_{\text{med},200}$, and R_{200} for stacking methods (i) (brown stars), (ii) (red crosses), and (iii) (orange circles), respectively. The vertical dotted line in each panel corresponds to the angular resolution of the y-maps. The width of each annulus is the same as the beam size, shown with the error bars along the x-axis. The error bars in the y-axes denote statistical+systematic 68% confidence intervals. See Section A.3 for details.

the individual radial bins are consistent within errors. In the intermediate $(10.4 < \log(M_{\star}/M_{\odot}) \leqslant 11.0)$ mass bins, the outer radial bins are more affected by the stacking methods than the innermost radial bin. In the most massive bin, the differences among the stacking methods, although present, are not visually prominent. Thus, it is crucial to incorporate the redshift and the virial radius into the stacking; otherwise, the signal might be incorrectly estimated. This is one of the major advancements in this work, as compared to previous studies.

Because the second stacking method involves information about the galaxy redshift while the first stacking method does not, the $\approx 16\%$ –45% scatter in D_A^{-1} in the individual mass bins causes the difference between the first and second stacking methods (see Equations (1) and (2)). The similar scatter in D_A^{-1} and in R_{200}/D_A (see Equations (2) and (3)) in all mass bins results in similar radial profiles for the second and third stacking methods. In further discussion, we consider the third stacking method only, because it takes into account the redshift and the virial radius, and the results using this method are the most straightforward to interpret in terms of the virial properties of galaxies.

Appendix B Radial Profiles of Compton-y

We show the stacked Compton-y maps, the posterior distribution of the model parameters, and the differential radial profiles of Compton-y along with the best-fitted model and its components in Figure B1. An excess in the $\approx 1-2 \times R_{200}$ region as compared to the region within R_{200} is visible in most of the y-maps stacked between $M_{\star}=10^{10.4}M_{\odot}$ and $M_{\star}=10^{11}M_{\odot}$, for different ΔM_{\star} . It leads to a flattening of the differential profile at a small radius, or even a deficit of Compton-y in the innermost radial bin as compared to the adjacent radial bin (visible in $M_{\star} = 10^{10.4-10.7} M_{\odot}$), which we refer to as a "central dip." We can visually identify such deviation from radially declining Compton-y only from differential profiles, not from cumulative profiles. The "central dip" could be an artifact due to the incomplete treatment of dust at the center of these galaxies, or a residual effect of fainter radio sources. Otherwise, it could happen due to galactic feedback snowplowing the CGM out of the halo. The "central dip" leads to an underestimated normalization of the pressure profile with weak constraints at the respective stellar mass bins, but it does not

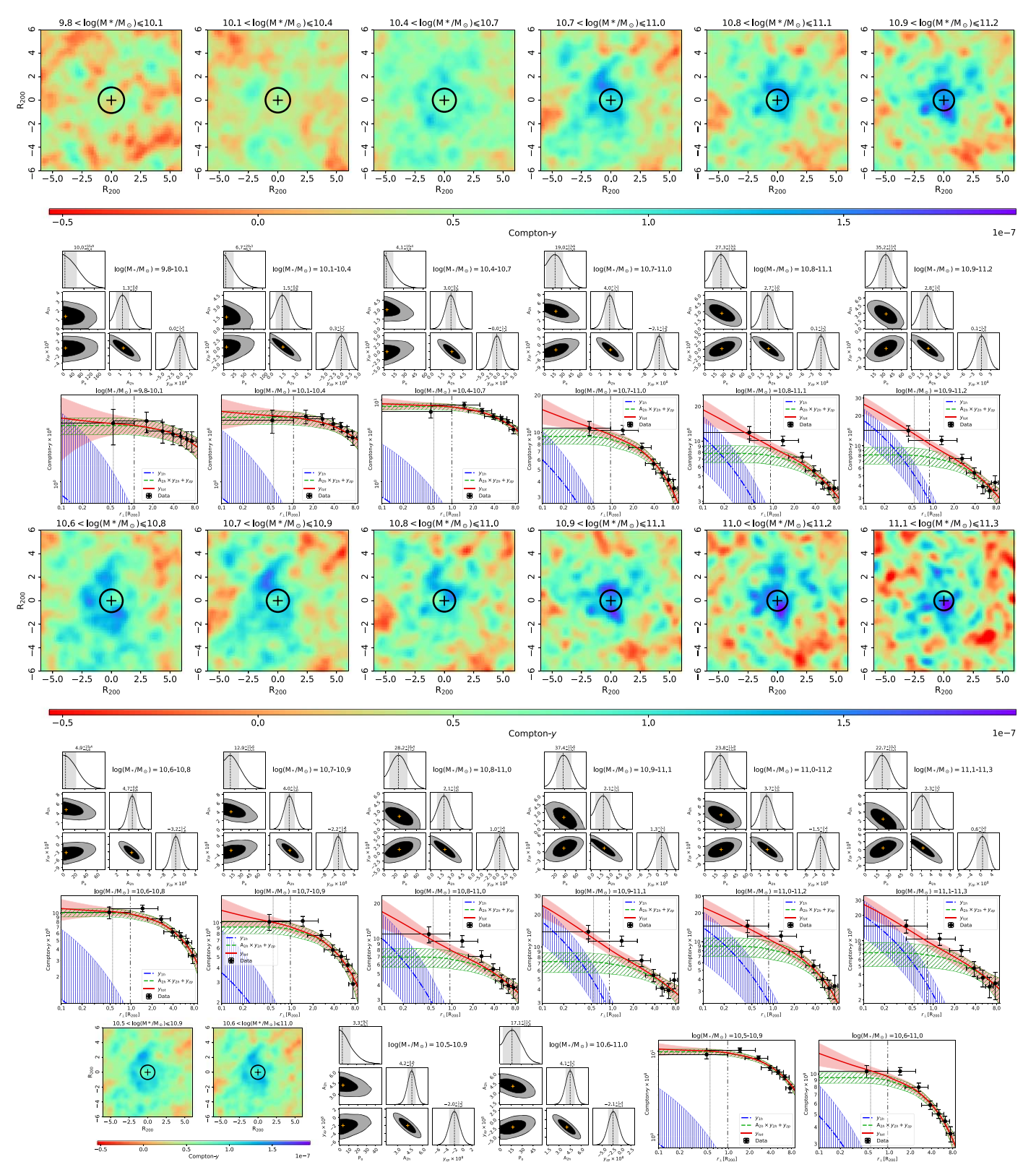


Figure B1. Stacked Compton-y maps; posterior probability distributions of P_0 , A_{2h} , and y_{zp} obtained by fitting the GNFW pressure model to our tSZ measurements; and differential radial profile of Compton-y. $\Delta M_{\star} = 0.3$ dex (top three rows), 0.2 dex (fourth, fifth, and sixth rows from top), and 0.4 dex (bottom row). The range of stellar mass is mentioned in the heading of each plot. See the top left, top right, and bottom left panels of Figure 5 for a more detailed description.

rule out the possibility of the Arnaud et al. (2010) pressure profile altogether. We will address the diversity in the shape of the radial profiles and its physical implications in a companion paper with advanced modeling.

Appendix C Central versus Satellite Galaxies

Central and satellite galaxies evolve in different environments; therefore they could have different SHMRs. The interpretation of our measured tSZ effect, and the quantities derived from it, would not be straightforward if our galaxy sample is dominated by satellite galaxies. In the following, we discuss the identification of central galaxies in our sample and the credibility of our analysis in the context of potential contamination from satellites.

We restrict the calculation to galaxy pairs that are at similar redshifts, i.e., whose photometric redshifts differ by less than their combined uncertainty in $z_{\rm ph}$: $|z_1-z_2|<\sqrt{(\sigma_{z_1}^2+\sigma_{z_2}^2)}$, where σ_z is the redshift uncertainty. By comparing $z_{\rm ph}$ with the corresponding spectroscopic redshifts from multiple catalogs, Bilicki et al. (2016) estimated the overall accuracy in $z_{\rm ph}$ to be $0.035\times(1+z_{\rm ph})$. We adopt it as an estimator of σ_z . If a galaxy is within $2\times\theta_{200}$ of a more massive galaxy, we identify it as a satellite of the more massive galaxy. We find that $\approx 37\%$ of our galaxy sample are central galaxies according to this condition.

To test the validity of our calculation of the fraction of central galaxies, f_{central} , we compare it with previous observational estimates or theoretical predictions of f_{central} . The halo occupation fraction of a central galaxy depends on the host halo mass. We calculate f_{central} as a function of stellar mass and virial mass using the occupation statistics prescription of Zheng et al. (2007) and Zu & Mandelbaum (2015), and show it in Figure C1.

Because the uncertainty in photometric redshift is large, the redshift difference between galaxies, and hence the number of galaxies to be considered as potential satellites, is large too. Therefore, our estimate of $f_{\rm central}$ is only a lower limit. The requirement of minimum angular distance, $\Delta\theta_{\rm min}$, between two central galaxies of $2\times\theta_{200}$ could be aggressive as well. In fact, a lenient requirement of $\Delta\theta_{\rm min}>\theta_{200}$ increases the overall $f_{\rm central}$ to \approx 71%. Given the size of our galaxy sample, the stacked signal over these central galaxies would be too weak to put a constraint on. Therefore, instead of restacking over the central galaxies, we compare existing prescriptions of $f_{\rm central}$ with our estimate of $f_{\rm central}$, and we try to understand how much our stacking results could be affected by satellite galaxies, if at all.

The exact dependence of $f_{\rm central}$ on mass is not of prime importance in our context. At a given stellar mass, if the speculated value of $f_{\rm central}$ (gray lines in Figure C1) is larger than the $f_{\rm central}$ of our galaxy sample (black squares), it would imply that our $f_{\rm central}$ is not underestimated, and hence, reliable. The exact measure of satellite galaxy contamination in our galaxy population is model-dependent and inconclusive. In the most conservative prescription of $f_{\rm central}$ (Zheng et al. 2007), the galaxy population is dominated by central galaxies at $>10^{10.6}M_{\odot}$, i.e., $f_{\rm central}>80\%$. Therefore, in the mass range where we can constrain the tSZ effect, it is safe to assume central galaxy properties in the interpretation of the results.

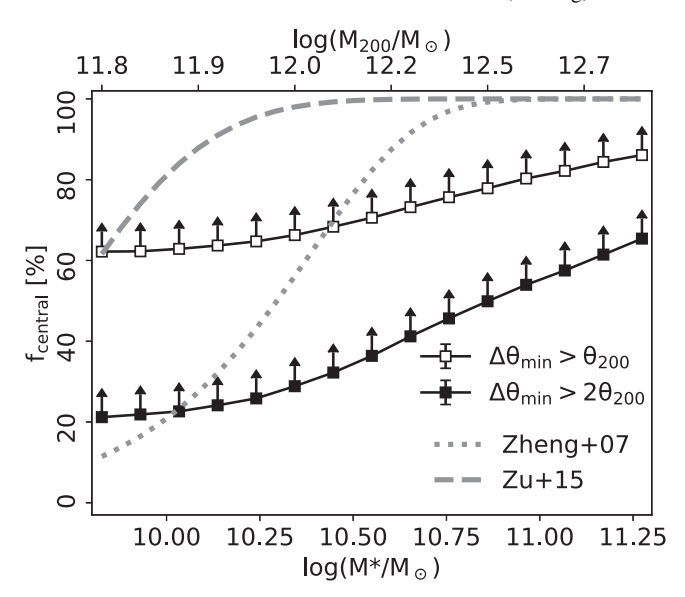


Figure C1. The fraction of central galaxies, f_{central} , as a function of the stellar mass (bottom x-axis) and virial mass (top x-axis). The black filled and unfilled squares are our calculated f_{central} in the WISE \times SCOSPZ galaxy sample for the requirement of minimum angular distance from more massive galaxies of $\Delta\theta_{\min} > 2\theta_{200}$ and $\Delta\theta_{\min} > \theta_{200}$, respectively. We show the speculated f_{central} for different halo occupation statistics with dotted (Zheng et al. 2007) and dashed (Zu & Mandelbaum 2015) curves.

ORCID iDs

Sanskriti Das https://orcid.org/0000-0002-9069-7061 Yi-Kuan Chiang https://orcid.org/0000-0001-6320-261X Smita Mathur https://orcid.org/0000-0002-4822-3559

References

```
Amodeo, S., Battaglia, N., Schaan, E., et al. 2021, PhRvD, 103, 063514
Anderson, M. E., Churazov, E., & Bregman, J. N. 2016, MNRAS, 455, 227
Arnaud, M., Pratt, G. W., Piffaretti, R., et al. 2010, A&A, 517, A92
Astropy Collaboration, & Astropy Project Contributors 2022, ApJ, 935, 167
Behroozi, P. S., Conroy, C., & Wechsler, R. H. 2010, ApJ, 717, 379
Bhattacharyya, S., Das, S., Gupta, A., Mathur, S., & Krongold, Y. 2023,
  arXiv:2208 07863
Bilicki, M., Peacock, J. A., Jarrett, T. H., et al. 2016, ApJS, 225, 5
Bluem, J., Kaaret, P., Kuntz, K. D., et al. 2022, ApJ, 936, 72
Bogdán, Á., Bourdin, H., Forman, W. R., et al. 2017, ApJ, 850, 98
Cen, R., & Ostriker, J. P. 1999, ApJ, 514, 1
Chadayammuri, U., Bogdán, Á., Oppenheimer, B. D., et al. 2022, ApJL,
Chiang, Y.-K., Makiya, R., Komatsu, E., & Ménard, B. 2021, ApJ, 910, 32
Chiang, Y.-K., Makiya, R., Ménard, B., & Komatsu, E. 2020, ApJ, 902, 56
Cluver, M. E., Jarrett, T. H., Hopkins, A. M., et al. 2014, ApJ, 782, 90
Comparat, J., Truong, N., Merloni, A., et al. 2022, A&A, 666, A156
Cortese, L., Ciesla, L., Boselli, A., et al. 2012, A&A, 540, A52
Das, S., Mathur, S., & Gupta, A. 2020, ApJ, 897, 63
Das, S., Mathur, S., Gupta, A., & Krongold, Y. 2021a, ApJ, 918, 83
Das, S., Mathur, S., Gupta, A., Nicastro, F., & Krongold, Y. 2021b, MNRAS,
  500, 655
Das, S., Mathur, S., Gupta, A., Nicastro, F., & Krongold, Y. 2019a, ApJ,
Das, S., Mathur, S., Gupta, A., et al. 2019b, ApJ, 885, 108
Das, S., Mathur, S., Nicastro, F., & Krongold, Y. 2019c, ApJL, 882, L23
Davies, J. J., Crain, R. A., Oppenheimer, B. D., & Schaye, J. 2020, MNRAS,
   491, 4462
Faucher-Giguere, C.-A., & Oh, S. P. 2023, arXiv:2301.10253
Foreman-Mackey, D. 2016, JOSS, 1, 24
Foreman-Mackey, D., Hogg, D. W., Lang, D., & Goodman, J. 2013, PASP,
```

125, 306

Gatuzz, E., & Churazov, E. 2018, MNRAS, 474, 696

Gelman, A., & Rubin, D. B. 1992, StaSc, 7, 457

```
Gommers, R., Virtanen, P., Burovski, E., et al. 2022, scipy/scipy: SciPy
   v1.8.0, Zenodo, doi:10.5281/zenodo.595738
Greco, J. P., Hill, J. C., Spergel, D. N., & Battaglia, N. 2015, ApJ, 808, 151
Gupta, A., Kingsbury, J., Mathur, S., et al. 2021, ApJ, 909, 164
Gupta, A., Mathur, S., Kingsbury, J., Das, S., & Krongold, Y. 2023, NatAs, 1
Gupta, A., Mathur, S., Krongold, Y., Nicastro, F., & Galeazzi, M. 2012, ApJL,
   756, L8
Harris, C. R., Millman, K. J., van der Walt, S. J., et al. 2020, Natur, 585, 357
Harrison, C. M. 2017, NatAs, 1, 0165
Hastings, W. K. 1970, Biometrika, 57, 97
Hearin, A., Tollerud, E., Robitaille, T., et al. 2016, Halotools: Galaxy-Halo
   connection models, Astrophysics Source Code Library, ascl:1604.005
Henley, D. B., Shelton, R. L., Kwak, K., Joung, M. R., & Mac Low, M.-M.
   2010, ApJ, 723, 935
Hilton, M., Sifón, C., Naess, S., et al. 2021, ApJS, 253, 3
Hopkins, P. F., Wetzel, A., Kereš, D., et al. 2018, MNRAS, 480, 800
Hunter, J. D. 2007, CSE, 9, 90
HI4PI Collaboration, Ben Bekhti, N., Flöer, L., et al. 2016, A&A, 594, A116
Kaaret, P., Koutroumpa, D., Kuntz, K. D., et al. 2020, NatAs, 4, 1072
Kashibadze, O. G., Karachentsev, I. D., & Karachentseva, V. E. 2020, A&A,
   635, A135
Kelly, B. C. 2007, ApJ, 665, 1489
Kim, J., Golwala, S., Bartlett, J. G., et al. 2022, ApJ, 926, 179
Kluyver, T., Ragan-Kelley, B., Pérez, F., et al. 2016, in Positioning and Power
   in Academic Publishing: Players, Agents and Agendas, ed. F. Loizides &
   B. Schmidt (Amsterdam: IOS Press), 87
Lara-DI, A. J., Krongold, Y., Mathur, S., Das, S., & Gupta, A. 2023, ApJ,
   946, 55
Lenz, D., Hensley, B. S., & Doré, O. 2017, ApJ, 846, 38
Li, J.-T., Bregman, J. N., Wang, Q. D., et al. 2017, ApJS, 233, 20
Li, J.-T., Bregman, J. N., Wang, Q. D., Crain, R. A., & Anderson, M. E. 2018,
       , 855, L24
Li, M., & Tonnesen, S. 2020, ApJ, 898, 148
Lim, S. H., Barnes, D., Vogelsberger, M., et al. 2021, MNRAS, 504, 5131
Lim, S. H., Mo, H. J., Li, R., et al. 2018, ApJ, 854, 181
Madhavacheril, M. S., Hill, J. C., Næss, S., et al. 2020, PhRvD, 102, 023534
Mathur, S. 2022, in Handbook of X-ray and Gamma-ray Astrophysics., ed.
   C. Bambi & A. Santangelo (Berlin: Springer), 59
Mathur, S., Gupta, A., Das, S., Krongold, Y., & Nicastro, F. 2021, ApJ,
   908, 69
```

Meinke, J., Böckmann, K., Cohen, S., et al. 2021, ApJ, 913, 88

```
Metropolis, N., Rosenbluth, A. W., Rosenbluth, M. N., Teller, A. H., &
  Teller, E. 1953, JChPh, 21, 1087
Mroczkowski, T., Nagai, D., Basu, K., et al. 2019, SSRv, 215, 17
Naess, S., Madhavacheril, M., & Hasselfield, M. 2021, Pixell: Rectangular
  pixel map manipulation and harmonic analysis library, Astrophysics Source
  Code Library, ascl:2102.003
Nagai, D., Kravtsov, A. V., & Vikhlinin, A. 2007, ApJ, 668, 1
Navarro, J. F., Frenk, C. S., & White, S. D. M. 1997, ApJ, 490, 493
Nelson, D., Kauffmann, G., Pillepich, A., et al. 2018, MNRAS, 477, 450
Neto, A. F., Gao, L., Bett, P., et al. 2007, MNRAS, 381, 1450
Nicastro, F., Krongold, Y., Fang, T., et al. 2023, arXiv:2302.04247
Nicastro, F., Senatore, F., Krongold, Y., Mathur, S., & Elvis, M. 2016, ApJ,
  828, L12
Pandey, S., Gatti, M., Baxter, E., et al. 2022, PhRvD, 105, 123526
Piffaretti, R., Arnaud, M., Pratt, G. W., Pointecouteau, E., & Melin, J. B. 2011,
   A&A, 534, A109
Pop, A.-R., Hernquist, L., Nagai, D., et al. 2022, arXiv:2205.11528
Putman, M. E., Peek, J. E. G., & Joung, M. R. 2012, ARA&A, 50, 491
Planck Collaboration, Ade, P. A. R., Aghanim, N., et al. 2013, A&A, 557,
Planck Collaboration, Ade, P. A. R., Aghanim, N., et al. 2016, A&A, 594, A13
Schaan, E., Ferraro, S., Amodeo, S., et al. 2021, PhRvD, 103, 063513
Schaye, J., Crain, R. A., Bower, R. G., et al. 2015, MNRAS, 446, 521
Shang, Z., Brotherton, M. S., Wills, B. J., et al. 2011, ApJS, 196, 2
Snowden, S. L., Freyberg, M. J., Kuntz, K. D., & Sanders, W. T. 2000, ApJS,
   128, 171
Spitzer, L. J. 1956, ApJ, 124, 20
Sunyaev, R. A., & Zeldovich, Y. B. 1969, Natur, 223, 721
The pandas development team 2020, pandas-dev/pandas: Pandas, v2.0 x series
  Zenodo, doi:10.5281/zenodo.3509134
Tumlinson, J., Peeples, M. S., & Werk, J. K. 2017, ARA&A, 55, 389
Van Rossum, G. 2020, The Python Library Reference, release 3.8.2 (Python
   Software Foundation)
Vavagiakis, E. M., Gallardo, P. A., Calafut, V., et al. 2021, PhRvD, 104,
Vikram, V., Lidz, A., & Jain, B. 2017, MNRAS, 467, 2315
White, R. L., Becker, R. H., Helfand, D. J., & Gregg, M. D. 1997, ApJ,
Williams, R. J., Mathur, S., Nicastro, F., et al. 2005, ApJ, 631, 856
Zheng, Z., Coil, A. L., & Zehavi, I. 2007, ApJ, 667, 760
Zu, Y., & Mandelbaum, R. 2015, MNRAS, 454, 1161
```